Axially decoupled photo-stimulation and two photon readout (*ADePT*) for mapping functional connectivity of neural circuits

Matthew Koh[1,2,#], Francesca Anselmi[2,#], Sanjeev K. Kaushalya[2,#], Diego E. Hernandez[2], Walter Germán Bast[2], Pablo S. Villar[2], Honggoo Chae[2], Martin B. Davis[2], Sadhu Sai Teja[2], Zhe Qu[3], Viviana Gradinaru[3], Priyanka Gupta[2, §], Arkarup Banerjee[1,2, §] & Dinu F. Albeanu[1,2,§]

1. CSHL School for Biological Sciences
2. Cold Spring Harbor Laboratory, Cold Spring Harbor, NY, 11724, USA
3. California Institute of Technology, Pasadena, CA, 91125

# - equal contribution

§ - Correspondence to: albeanu@cshl.edu; banerjee@cshl.edu; pgupta@cshl.edu

Key words: *patterned photo-stimulation, digital micro-mirror device, holographic diffuser, two photon microscopy, all-optical physiology, 3-D functional connectivity mapping, olfactory bulb, sister mitral/tufted cells, short axon cells*

Abstract

All optical physiology *in vivo* provides a conduit for investigating the function of neural circuits in 3-D. Here, we report a new strategy for flexible, axially-decoupled photo-stimulation and two photon readout (*ADePT*) of neuronal activity. To achieve axially-contained widefield optogenetic patterned stimulation, we couple a digital micro-mirror device illuminated by a solid-state laser with a motorized holographic diffuser. In parallel, we use multiphoton imaging of neural activity across different z-planes. We use *ADePT* to analyze the excitatory and inhibitory functional connectivity of the mouse early olfactory system. Specifically, we control the activity of individual input glomeruli on the olfactory bulb surface, and map the ensuing responses of output mitral and tufted cell bodies in deeper layers. This approach identifies cohorts of *sister* mitral and tufted cells, whose firing is driven by the same parent glomerulus, and also reveals their differential inhibition by other glomeruli. In addition, selective optogenetic activation of glomerular GABAergic/dopaminergic (DAT+) interneurons triggers dense, but spatially heterogeneous suppression of mitral and tufted cell baseline activity and odor responses, further demonstrating specificity in the inhibitory olfactory bulb connectivity. In summary, *ADePT* enables high-throughput functional connectivity mapping in optically accessible brain regions.

Introduction

Manipulating select neural circuit elements is critical for understanding the circuit mechanisms underlying brain computation, especially when coupled with activity monitoring and behavioral analysis. In recent years, optogenetic control of specific cell-types has been widely adopted as a method of choice[1–5], and various combinations of optical imaging and spatial light patterning techniques[6–19] have achieved concurrent stimulation and activity recording, typically in the same optical z-plane. This is primarily constrained by the microscope anatomy, as the photo-stimulation and imaging light paths converge onto the sample through a shared microscope objective which focuses both the stimulation and imaging light patterns in its fixed focal plane. Neuronal circuits are however distributed in 3-D and investigating the functional connectivity of such neural circuits requires flexible control and readout of neural activity in independent optical planes (e.g. stimulating layer 1 dendrites and monitoring neuronal activity in layers 5, **Fig. 1a**).

Several strategies have been developed over the past two decades to target multiple optical z-planes simultaneously, or in quick succession. These range from dual scanning head implementations[19] to using tunable focusing elements (e.g. electrically-tunable lenses, ETL) whose focal length can be dynamically controlled[20–22], acousto-optic deflector (AOD)-based arbitrary access imaging systems[14,23–28] and digital holography[8,9,13,27,29–33]. These methods have varying trade-offs, and to date, monitoring and photo-activating neurons in three dimensions remains challenging. When choosing an adequate photo-stimulation and imaging approach, several aspects are worth considering: the required spatial resolution in 3-D (stimulating individual cell bodies versus extended patches of tissue), the size of the field of stimulation, the axial separation between the stimulation and imaging planes (relative locations of the input-output nodes

of the circuit), the cost and simplicity of implementation and its robustness. Early scanning-based methods enabled photo-stimulation over large fields of view (FOVs), but conferred poor axial resolution[34,35], potentially leading to off target photo-activation in 3-D. In contrast, modern methods achieved flexible and precise 3-D confinement of photo-stimulation using AOD-based approaches, or digital holography in combination with temporal focusing[8,9,13,27–33]. AOD-based and holographic control of activity, however, can be technically challenging and cost-prohibitive, and the size of the field of photo-stimulation is limited by steep power requirements. Axial decoupling between the stimulation and imaging planes has also been achieved by simpler methods such as using ETLs, but these implementations are constrained by spherical aberrations which deteriorate the point spread function and limit the size of the field of stimulation.

Here we introduce *ADePT* (Axially Decoupled Photo-stimulation and Two-Photon readout), an easy implementable, cost-effective and high-throughput technique that combines one-photon widefield patterned illumination with multiphoton imaging in axially decoupled planes (**Fig. 1b**). Our approach enables precise axially-confined photo-stimulation, with arbitrarily shaped light patterns, across an extended region on the brain surface, while imaging neuronal activity in other optically accessible z-planes of choice. We use a digital micro-mirror device (DMD)[17,36–46] to impose customizable 2-D spatial patterns onto a Gaussian laser beam that are subsequently optically relayed onto the sample. Due to the coherent nature of the illumination source (laser), the spatial patterning is maintained throughout the optical path between the DMD chip and the sample (infinite focus). Placing a (holographic) diffuser in the optical path breaks the coherence and disrupts this infinite focus. The desired 2-D pattern comes into focus only in an axially confined optical-plane in the sample that is conjugate to the diffuser. To flexibly target photo-stimulation

92 across different depths in the sample, independent of the multiphoton imaging plane (objective's
93 focal plane), we simply translate the diffuser along the optical path using a motorized stage. Akin
94 to remote focusing imaging approaches[16,20,47–52], translating the diffuser displaces the optical z-
95 plane within the sample where the stimulation pattern is in focus independent of the objective's
96 focal plane (**Fig**. **1c**). In our implementation, we report ~20 µm lateral (17.1 µm x-y-FWHM) and
97 ~40 µm axial (36.3 µm z-FWHM) resolution of the patterned photo-stimulation across a 1.2 x 1.5
98 mm field of stimulation (20X, 1.0 NA, Olympus objective). We calibrated this method across up
99 to 500 µm axial displacement between the photo-stimulation plane and the focal plane of the
100 objective. Note that these parameters are not strictly rigid, and *ADePT* can accommodate many
101 different operating configurations depending upon the specific biological application.
102
103 We subsequently assessed the effectiveness of *ADePT* for investigating the logic of circuit
104 connectivity by leveraging the 3-D spatial layout of the mouse olfactory bulb (OB)[53,54]. In the OB,
105 the input nodes called glomeruli (balls of neuropil sorted by odorant receptor identity) and the
106 principal output neurons (mitral and tufted cells) are separated by approximately two hundred
107 microns in depth. We investigated the excitatory and inhibitory logic of this early olfactory circuit
108 by photo-stimulating either the glomeruli or local inhibitory interneurons while monitoring
109 responses of mitral/tufted cells (MT cells). We found that *sister* OB output neurons[36,55–65] – those
110 that receive primary input from the *same* 'parent' glomerulus – differ substantially in their lateral
111 inhibitory connectivity with other glomeruli with the OB network, potentially explaining their non-
112 redundant responses to odors[36,55]. Further, we found that local GABAergic/dopaminergic
113 interneurons[42,43,66–74] associated with different glomeruli provide dense, but selective inhibition to
114 regulate odor responses of OB output neurons. In summary, *ADePT* is readily-deployable and well-

suited for high-throughput mapping of both excitatory and inhibitory functional connectivity in optically accessible brain regions.

Results

Design of the axially decoupled patterned photo-stimulation and imaging setup

We couple a custom laser scanning two photon microscope (Methods) with a modular add-on for axially-contained widefield (one-photon) patterned photo-stimulation (**Fig**. **1b**). Patterned photo-stimulation is achieved using a digital micro-mirror device (VX4100 DMD, 0.7" XGA VIS 1024 x 768 pixels, 13.68 µm micro-mirror pitch, Vialux) illuminated by a solid-state CW laser (Sapphire, 488 nm, 200 mW, Coherent). The photo-stimulation and two-photon excitation paths are combined using a dichroic mirror (680dcxr, 50 mm diameter, Chroma) placed above the objective (20X, 1.0 NA, Olympus). A diffuser mounted on a motorized translation stage enables flexible control of the axial location of the photo-stimulation plane in the sample (**Figs**. **1a-c**). Without the diffuser, the photo-stimulation 2-D pattern is in focus throughout the optical path as pencils of coherent light (**Fig**. **1c**, *Top*). By placing the diffuser in the optical path, the coherence of the beam is disrupted and the 2-D spatial pattern imposed by the DMD is accurately reconstructed in the sample only in a thin (axially-contained) image plane. This image plane is optically conjugated with both the diffuser and the DMD chip. In the default 4f configuration, the DMD pattern thus comes into focus in the focal plane of the objective such that the photo-stimulation and multiphoton imaging planes overlap axially (**Fig**. **1c**, *Middle*). Importantly, translating the diffuser along the optical path causes its conjugate image plane in the sample to move as well, therefore axially decoupling the photo-stimulation plane from the focal (sample) plane of the imaging objective (**Figs**. **1b-c**, *Bottom*, **S1a-b**).

Introducing a diffuser in the optical path has the added benefit of improving the axial confinement of the photo-stimulation pattern. The diffuser breaks the coherence of the DMD-modulated laser pattern, dispersing light across a solid angle (Methods). As the photo-stimulation pattern in the sample plane is a conjugate image of the diffuser, it is expected to be restricted to a thin optical z-plane and its axial extent to scale linearly with the lateral (x-y) spot size[6,12,75]. Note that this differs from the focusing regime of a Gaussian laser beam where the axial extent of the focal spot increases quadratically with the lateral extent of the spot. In *ADePT*, the axial confinement of the photo-stimulation pattern depends directly on the available light angles emerging from the diffuser (effective numerical aperture): the wider the cone of angles, the tighter the axial confinement (higher axial resolution) albeit with increased loss of excitation light.

Figure 1

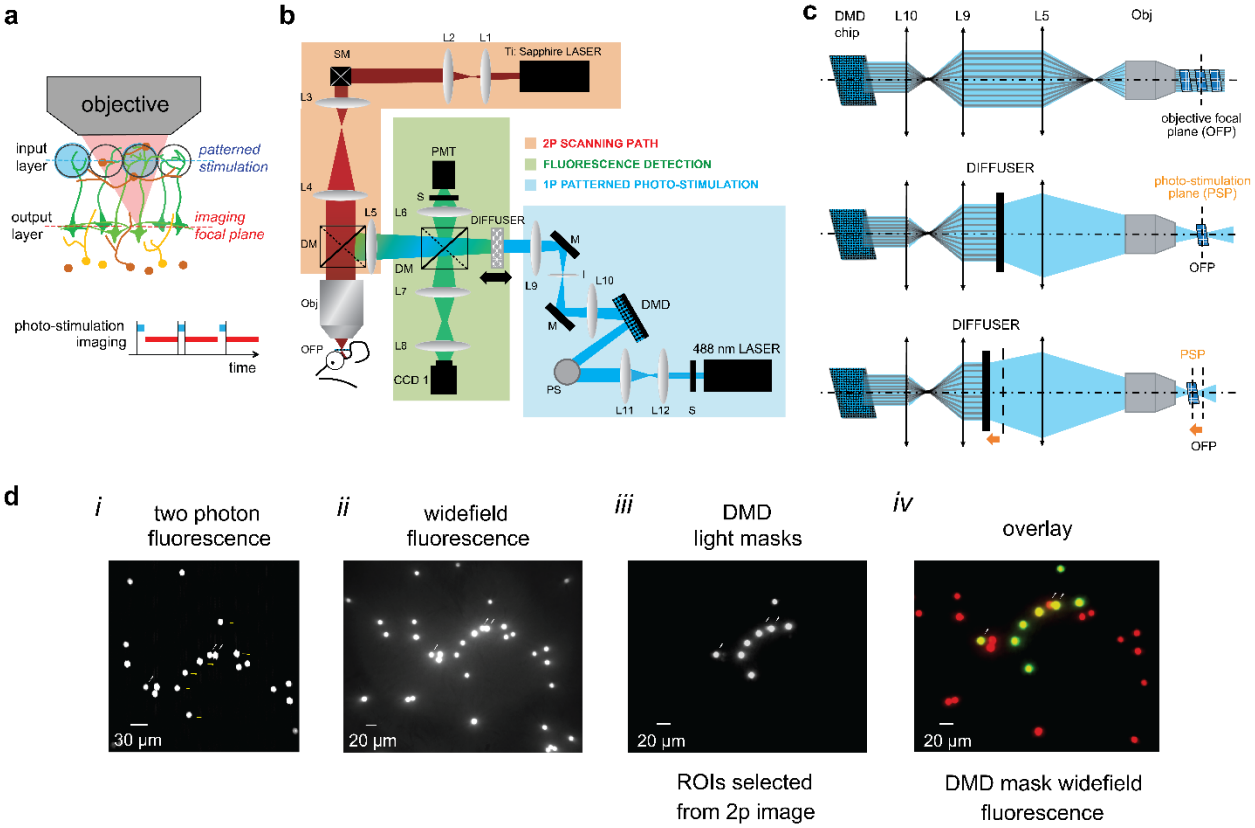

Figure 1: Axially decoupled patterned photo-stimulation and multiphoton imaging. (a) *(Top) Cartoon schematics of functional connectivity mapping of a neural circuit (e.g. olfactory bulb);*

*photo-stimulation (2-D light mask from a digital micro-mirror device illuminated with a solid-state CW laser) and two photon imaging are confined to different optical z-planes that can be flexibly and independently adjusted by translating the diffuser and respectively the primary objective; (Bottom) Alternating (strobing) between photo-stimulation and imaging periods. Each red bar represents a single frame of multiphoton imaging. Photo-stimulation and imaging periods are interleaved. (**b**) Microscope schematics. DM, dichroic mirrors. DMD, digital micro-mirror device. I, iris diaphragm. L1-L12, lenses. O, primary objective. PMT, photomultiplier tube. PS, periscope. S, shutter. SM, scan mirrors. (**c**) (Top) Illustration of using a movable diffuser to decouple the patterned photo-stimulation and multiphoton imaging planes. The diffuser is imaged into the sample, in a 4f lens configuration; translating the diffuser along the optical path causes the corresponding projection plane to shift axially. OFP, objective focal plane. PSP, photo-stimulation plane. (**d**) DMD chip-to-CCD camera-to-2p microscope registration. (i) two photon micrograph of 10 µm fluorescence microbeads; arrows mark two microbeads, part of the larger DMD-modulated projection target pattern (8 microbeads), which were taken as fiduciary points; (ii) widefield fluorescence image (full field illumination) of a larger field of view including the target microbeads; (iii) ROIs selected from the 2p image were used to generate DMD-chip light masks; these were further projected at the primary objective focal plane and imaged using the primary CCD camera (CCD 1); (iv) overlay of DMD-generated photo-stimulation masks and widefield fluorescence image of 10 µm microbeads from (ii); note that fluorescence is restricted to the microbeads targeted by the DMD photo-stimulation masks with minimal spillover to adjacent (off-target) microbeads (see fiduciary marks).*

We registered the DMD field of stimulation (DMD pixel size = 2.4 µm at the sample, **Fig**. **1d**) to the primary CCD camera image (CCD1 pixel size = 1.1 µm at sample; CCD 1300-QF, Vosskuhler) and the multiphoton field of imaging into a common reference frame (Methods). We verified that the targeting of DMD-modulated spatial light patterns was precise (< 5 µm error, note that fluorescence is restricted to the microbeads targeted by the DMD photo-stimulation masks with minimal spillover to adjacent, off-target microbeads, **Fig**. **1d**, **2b**, **S1d**). To ensure flat photo-stimulation probability across the field, we measured and further corrected light power inhomogeneities arising due to the Gaussian profile of the photo-stimulation laser beam and aberrations along the optical path (**Fig. S1e**). In control experiments (no fluorescent sample), we observed unwanted phosphorescence upon photo-stimulation, depending on the lens material (BK7 vs. fused silica). Consequently, we compared different objective and lens combinations and

chose the primary objective (20X, 1.0 NA, Olympus) and collection tube lens (L5; 100 mm FL, fused-silica, LA4545-A, Thorlabs) such as to minimize these artifacts (**Fig**. **S1f**, Methods).

Lateral and axial resolution of photo-stimulation

To determine the lateral and axial resolution of photo-stimulation setup, we projected light spots of increasing nominal diameters onto a glass coverslip spin-coated with 1µm thick rhodamine B layer (**Figs**. **2**,**3**). We measured the resulting fluorescence signals by imaging the rhodamine-coated coverslip from below with an inverted (secondary) microscope. The secondary microscope was set up so as to be confocal with the primary microscope objective (**Figs**. **2a-c**, **3a**)[6]. Each spot was sampled through the fluorescent coverslip by moving the primary objective up or down in steps of 1-2 µm. We used the images acquired by the primary (CCD1) and secondary (CCD2) cameras (**Fig**. **3a**; CCD1300QF, Vosskuhler) to obtain the lateral (x-y) and axial (z) extent of the light intensity profile at full width half maximum (FWHM, **Figs**. **2b-c**, **S2a-b**). Using this strategy, the smallest resolvable photo-stimulation spot we achieved was ~20 µm in lateral diameter (17.1 µm FWHM, **Figs**. **2b**, **S2a-b**). Below this size, decreasing the nominal spot size did not change the measured x-y-FWHM of the spot, potentially due to light scattering from the extended spot, light loss and imperfections in the setup's optical transfer function.

We further investigated the effect of the choice of diffuser on the z-FWHM for projected light spots of different sizes. As reported previously for light patterning techniques such as digital holography[6,12,75], we observed a linear dependence between the axial and lateral extent of the light patterns projected (z-FWHM vs. x-y-FWHM of photo-stimulation spots, **Fig**. **2c**). As expected, the ratio between the axial vs. lateral resolution was inversely proportional to the diffuser

divergence angle (slope = 1.52 when using a *grit ground* diffuser, #38-786 vs. 1.62 for a 10° *holographic* diffuser, #48-506 vs. 2.12 for a 5° *holographic* diffuser, #55-849, Edmund Optics, **Fig**. **2c**). In other words, the axial spread of the projected light pattern increased as the diverging angle of the *holographic* diffuser got narrower (lower NA). To minimize excitation light loss while maintaining ~40 µm axial resolution, we settled on a 5° *holographic* diffuser, a diffractive optical element designed to limit the spread of transmitted light to a specified solid angle (e.g., 5°, #55-849, Edmund Optics, **Fig**. **2c**). Using a 5° *holographic* diffuser only slightly under-filled the angular aperture of the primary objective and did not affect the lateral resolution of the system. Using a 10° *holographic* diffuser, or a *grit ground* diffuser would further increase the axial specificity (~30 µm) at the expense of light loss.

Figure 2

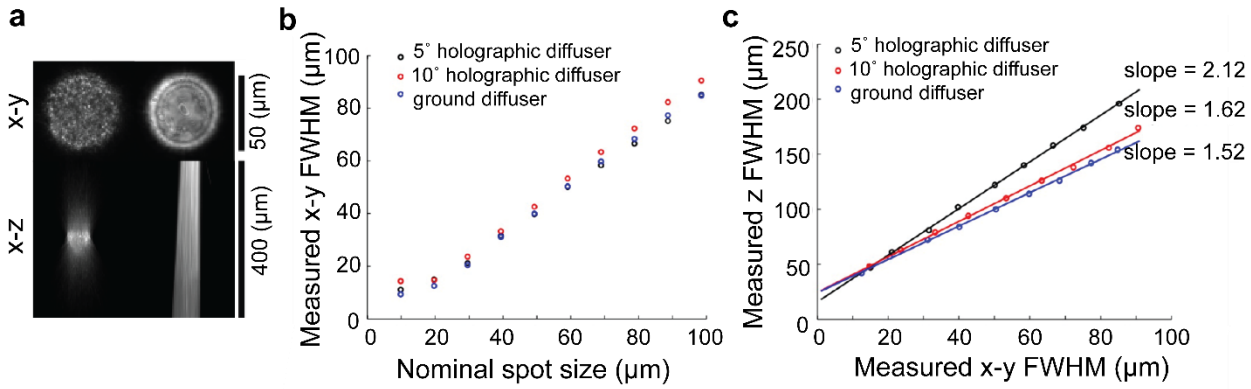

Figure 2. Axial confinement and resolution of the patterned stimulation and multiphoton imaging setup. ***(a)*** *Axial confinement of light intensity of a 2-D projection pattern using a holographic diffuser conjugated to the focal plane of the principal objective (Left) vs. same optical configuration without a diffuser (Right); spot diameter = 50 µm.* ***(b)*** *Measured spot x-y FWHM versus expected nominal spot size calculated by multiplying the pattern size in pixels by the expected size of a pixel given the DMD chip and the optical magnification of the system. Circular spots of different sizes (10-100 µm in diameter) were projected on a glass slide coated with a 1µm thin layer of rhodamine B.* ***(c)*** *Measured axial (z) FWHM versus lateral (x-y) FWHM of the projected spots from (**b**) for three different types of diffusers; black circles = 5˚ holographic diffuser; red circles = 10˚ holographic diffuser; blue circles = grit ground diffuser.*

192 **Decoupling imaging and photo-stimulation across different z-planes**

193 To flexibly manipulate the relative positioning of the photo-stimulation plane with respect to the
194 multiphoton imaging plane, we physically translate the diffuser on a motorized stage (**Fig. 1b**).
195 Theoretically, we expect a linear relationship between the axial displacement of the objective and
196 the corresponding compensatory displacement of the diffuser that is proportional to the square of
197 the magnification of the optical system (Eqs. 1-5, Methods). To verify and experimentally calibrate
198 the decoupling of photo-stimulation and imaging planes across a range of depths in our setup, we
199 projected a checker-board light pattern on a fluorescent coverslip coated with a ~1 µm thin layer
200 of rhodamine B. We imaged the resulting fluorescence through both the primary microscope and
201 a secondary inverted widefield microscope placed below (**Fig. 3a**)[6]. In the default configuration,
202 the diffuser is conjugate to the sample (objective focal plane), the secondary objective is confocal
203 with the primary objective, and the rhodamine coverslip is placed in their shared focal plane (also
204 the sample plane). The photo-stimulated pattern thus appears in focus on both CCD1 (primary
205 objective) and CCD2 (secondary objective). As we lowered the primary objective, as one would
206 to image deeper structures in a sample, the projected pattern also moved lower (below the
207 coverslip). This can be observed as a blurred image of the photo-stimulation pattern on CCD2 as
208 its imaging plane is still conjugate to the rhodamine coverslip. We determined the extent of the
209 diffuser displacement necessary to re-focus the projected pattern back onto the original plane of
210 interest in the sample (the rhodamine coverslip) by translating the diffuser away from the objective
211 until a sharp image of the checker-board reappeared on CCD2 (**Fig. 3a**). Moving down the primary
212 objective by incremental amounts (100 µm) and monitoring the required diffuser displacement via
213 the secondary microscope, we obtained a calibration curve, describing the effective decoupling of

the imaging and photo-stimulation planes up to 500 µm (i.e. spanning the 50 mm range of a Newport 433 translation stage we used to mount the diffuser, Methods, **Fig**. **3b**).

As the photo-stimulation pattern was moved away from the focal plane of the objective, we measured a slight increase in lateral (<10%) and axial extent (<20%, **Fig**. **3c**), which we further accounted for by applying corrections in the control software (Methods). Over the axial displacement interval sampled, we observed a linear relationship between translating the objective axially and the compensatory displacement of the diffuser required to bring the pattern back into focus, proportional to the square of the effective optical magnification in our setup (theoretical vs. effective magnification ~11.1 X vs. ~9.3 X, **Fig**. **3b**, Methods).

Figure 3

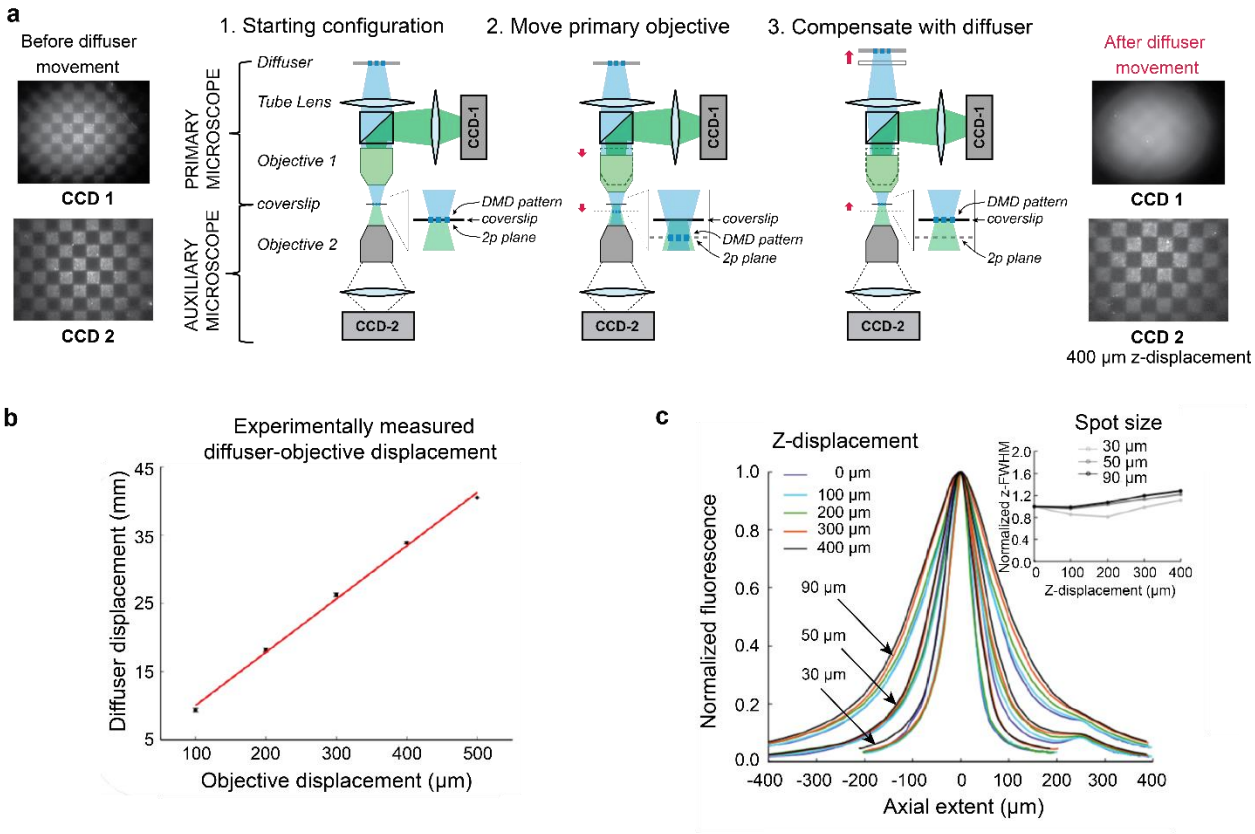

Figure 3. Decoupling the photo-stimulation and imaging z-planes using a translatable diffuser. ***(a)*** *Schematic cartoon describing using of the primary and secondary (auxiliary) microscopes to calibrate the decoupling of the photo-stimulation and optical-readout planes. A thin (1 µm) rhodamine B fluorescent coverslip sample is placed in the focal plane of both primary and*

secondary microscope objectives, where a checker-board pattern is projected using the DMD-chip (Step 1). Lowering the primary objective by a given amount translates the pattern axially below the focal plane of the secondary objective (which remained stationary), and produces a blurred image of the checker-board pattern on the secondary (CCD2) camera (Step 2). The projected light pattern is brought back into focus on CCD2 by compensating with translating the diffuser along the optical path (i.e. moving the diffuser away from the back-aperture of the primary objective, which defocuses the image on the primary (CCD1) camera (Step 3). ***(b)*** *Measured calibration curve of diffuser translation required to shift photo-stimulation plane by a given amount with respect to the focal plane of the objective. Each point represents Mean ± SEM across several months, indicating the robustness of the setup and linear relationship between objective and compensatory diffuser displacements for the range of photo-stimulation and imaging plane decoupling sampled (500 µm).* ***(c)*** *Normalized axial light intensity profile of spots. Measurements for spots of three different diameters (30, 50 and 90 µm), indicated by the three clusters of color traces. Each line color represents a different diffuser offset, expressed as degree of axial displacement between the photo-stimulation and focal plane of the primary objective in 100 µm steps (0 to 400 µm). (Inset) Measured change in axial (z) FWHM of the light profiles in* ***c.*** *as a function of axial displacement between photo-stimulation and imaging planes relative to no-offset (z-overlapping) condition, which we further accounted for by applying corrections in the control software.*

Quantifying photo-stimulation pattern propagation through brain tissue

One-photon patterned stimulation is constrained to surface applications because of limited penetration of shorter wavelengths into tissue due to scattering. To characterize the propagation of DMD-generated light patterns through brain slices of different thickness[76,77], we placed fixed olfactory bulb slices (Methods) atop a fluorescent coverslip, and recorded images of the projected patterns from underneath with the auxiliary microscope. To reduce the effect of variability in slicing angle and local neuronal architecture, we acquired images at two axial locations in each slice (Methods). Patterns remained distinct in slices up to ~150 µm thick (**Figs**. **S2c-f**), albeit substantial fluorescence loss (**Fig**. **S2f**). We note that using the diffuser, besides confining the axial spread of photo-stimulation, also increases the homogeneity of the projected light patterns in scattering media (**Figs**. **S2f-g**). Without the diffuser in the optical path, patterns appeared speckled: standard deviation of pixel intensities within the pattern was higher compared to same thickness samples with the diffuser in place (**Figs**. **S2e-g**). This effect can be explained intuitively by taking

a ray-tracing point of view on image formation. With the diffuser in the optical path, due to angular dispersion, light emitted from a single point in the pattern travels along more paths through the tissue compared to the no-diffuser condition to reach at a given camera pixel (**Fig**. **S2e**). As such, using the diffuser increases homogeneity in light intensity across the field of stimulation, as this configuration is less sensitive to variations in scattering from local structure in the tissue.

Mapping functional connectivity in the intact brain

ADePT combines precise, patterned optogenetic stimulation of the brain with high-resolution monitoring of resultant neuronal activity. This method is ideal for investigating the logic of functional connectivity in layered neuronal circuits where input and output circuit elements do not necessarily lie in the same plane. In addition, our one-photon DMD based implementation is particularly well-suited for understanding information flow in areas where sensory stimuli evoke structured spatiotemporal patterns of activity that extend over several 10s of microns (e.g. glomeruli in the olfactory, whisker barrels in barrel cortex, etc.). As a proof of principle, we used *ADePT* to investigate the role of different local inhibitory and excitatory connections in shaping the output of the mouse olfactory bulb. Briefly, in the OB, the input nodes called glomeruli (balls of neuropil sorted by odorant receptor identity) and the cell bodies of the principal output neurons (mitral and tufted cells) are separated by a couple hundred micrometers in depth[53,54]. Individual odors activate distinct spatial-temporal combinations of glomeruli. This odor-evoked activity is heavily reformatted within the OB by numerous excitatory and inhibitory interneurons and relayed to other brain areas in the form of activity patterns of the mitral/tufted cells. To date, understanding the OB computations has been challenging due to constraints in precisely and flexibly controlling the activity of individual input nodes (glomeruli) using traditional odor stimuli. Using *ADePT* we

can bypass these constraints by direct photo-stimulation while simultaneously monitoring the OB outputs at high throughput and cellular resolution.

Application 1: Mapping glomerular receptive fields of sister mitral/tufted cells

We used *ADePT* to first identify cohorts of *sister* output cells in the OB – mitral and tufted cells that receive excitatory input from the same *parent* glomerulus[36,55–64] – and then assess whether they integrate lateral inputs from different sets of glomeruli in the OB. Indeed, *sister* mitral and tufted cells extend multiple secondary (lateral) dendrites, which may each contact different sets of inhibitory interneurons[36,55,56,78]. Previous work has shown that while *sister* cells are generally responsive to the same set of odors, they are not redundant in their odor responses: pairs of *sister* cells are as different as pairs of *non-sisters* in their response time with respect to inhalation onset[36,55]. A potential mechanism for temporal differences in the odor-evoked responses of *sister* cells is differential inhibitory inputs from other glomeruli in the OB. However, to date, mapping glomerular receptive fields of individual mitral/tufted cells has been difficult given technical limitations in precise control of single-glomerulus activity in conjunction with monitoring responses at a high-enough yield to identify and further compare cohorts of *sister* mitral/tufted cells. Using *ADePT* enabled us to bypass the constraints imposed by odor stimulation and directly photo-stimulate individual glomeruli on the OB surface. In parallel, it enabled monitoring the responses of many mitral/tufted cells simultaneously at cellular resolution using multiphoton calcium imaging. To this end, we used mice expressing both an opsin in the mature olfactory sensory neurons (OSN), OMP-Cre x ReaChR-mCitrine[79] and the genetically encoded calcium indicator (GCaMP6f/s[80]) in the mitral and tufted cells (Thy1-GCaMP6s[81]; **Fig. S3a**, Methods).

Figure 4

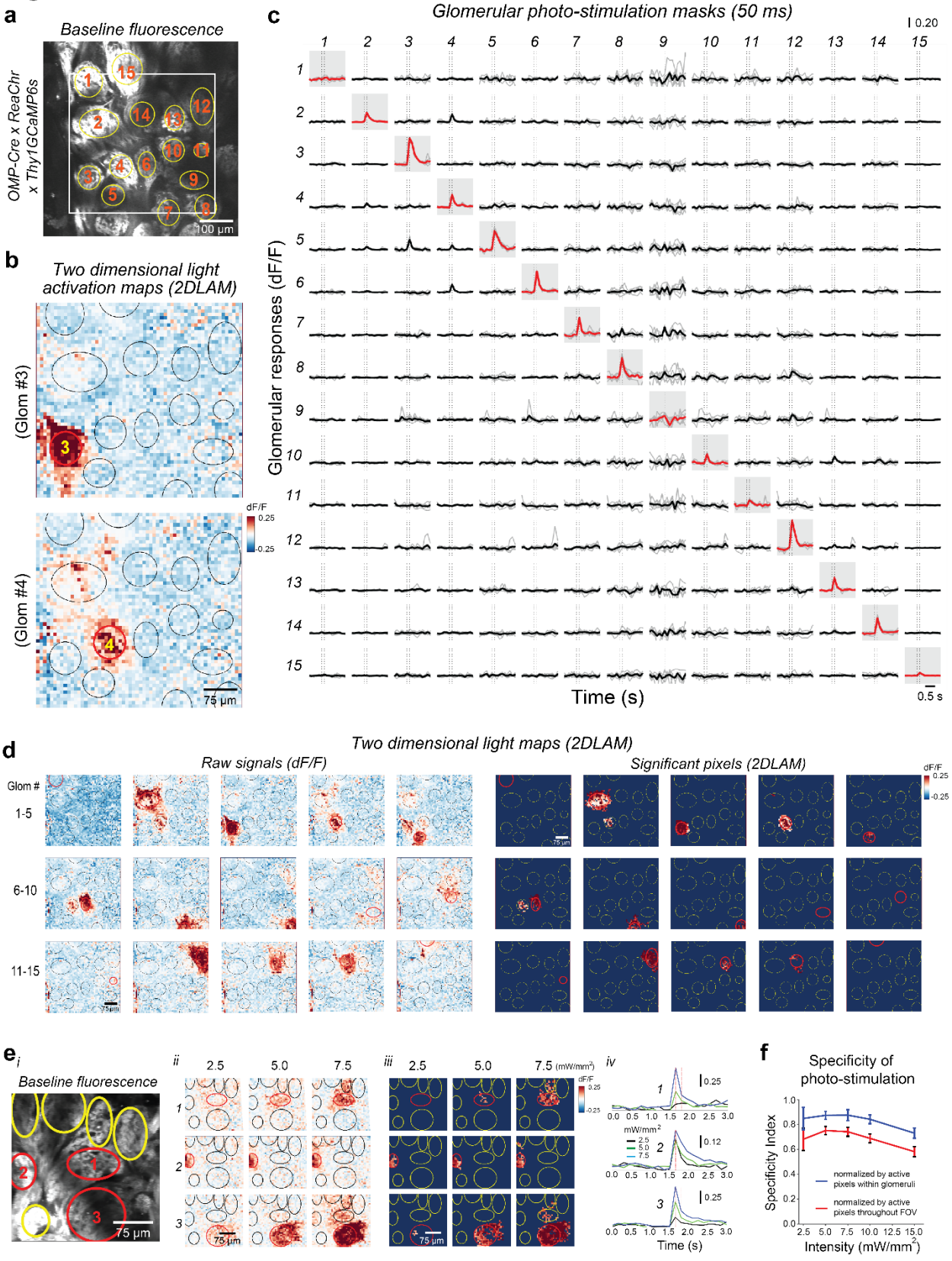

281

Figure 4. Targeting individual glomeruli by photo-stimulation of olfactory sensory neuron terminals and monitoring glomerular responses of sister mitral and tufted cell dendrites. (a) *(i) Glomerular resting fluorescence in OMP-Cre x ReaChR-citrine x Thy1-GCaMP6s mice;* ***(b)*** *Fluorescence changes (two dimensional glomerular light activation maps, 2DLAMs) evoked by photo-stimulation of 2 example glomeruli (#3, #4) out of 15 glomeruli targeted in the example field of view (5.0 mW/mm^2 for 50 ms). Red ellipses mark the location and contour of the projected light masks. Color scale in heat map indicates ΔF/F, comparing fluorescence after light stimulation to baseline;* ***(c)*** *Response matrix of fluorescence traces (individual repeats in gray, and mean signal as thicker lines) corresponding to 15 glomerular regions of interest versus the 15 (matching) glomerular light masks projected on the OB surface. Red traces mark responses of the targeted glomerulus in a given trial.* ***(d)*** *(Left) Fluorescence changes (two dimensional glomerular light activation maps, 2DLAMs; 5.0 mW/mm^2) evoked by photo-stimulation of the 15 glomeruli targeted in the example field of view (**a**). (Right) Significant 2DLAMs. Non-significant responses were thresholded to blue background. Out of 15 targeted glomeruli, 5 glomeruli were considered non-responsive, given our signal threshold criteria (Methods). Of the 10 responsive light maps, 8 showed specific responses (pertaining to the target glomerulus), and 2 light maps were not specific (responses were observed across multiple glomeruli).* ***(e)*** *Example target glomeruli from a different example FOV across a range of three light intensities (2.5, 5.0 and 7.0 mW/mm^2). Projected light masks match the red ellipses in (i) and (ii). Color scale in heat map indicates ΔF/F, comparing fluorescence triggered by light stimulation to baseline; (iii) Same as (ii) for statistically significant glomerular photo-stimulation responses (rectified 2DLAMs); (iv) Fluorescence traces (mean signal for each light intensity) corresponding to three regions of interest (ROI) in each heat map, whose position is indicated by red ellipses in i-iii. Different intensities are represented by different color traces (red - 2.5mW/mm^2, green - 5.0mW/mm^2, blue - 7.5mW/mm^2).* ***(f)*** *Specificity of glomerular responses across light intensity. Blue trace: responsive pixels within the target glomerulus normalized by all responsive pixels located within glomerular boundaries across the FOV. Red trace: responsive pixels within the target glomerulus normalized by all responsive pixels within the FOV, including those spanning the juxtaglomerular space, surrounding glomeruli (Methods); N=7 mice, 21 FOVs; responsive vs. photo-stimulated glomeruli: 2.5mW/mm^2, 12/74; 5.0mW/mm^2, 48/122; 7.5mW/mm^2, 27/57; 10.0mW/mm^2, 48/98; 15.0mW/mm^2, 48/77.*

We stimulated glomeruli by projecting DMD-modulated light masks on top of individual glomeruli, identified based on their baseline fluorescence (Methods). We used photo-stimulation spot sizes smaller (30-50 µm) than the targeted glomeruli (Avg. ~75 µm)[36,82]. To assess the resultant responses in the mitral/tufted cells, we strobed between stimulating OSN axon terminals (50-150 ms stimulation) and monitoring calcium responses (5-10 Hz imaging rate) in either the postsynaptic mitral/tufted dendritic tufts in the glomerular layer (same z-plane) or the cell-bodies (100-270 µm below the photo-stimulation plane). First, we calibrated the stimulation light intensity to ensure single glomerulus specificity – photo-stimulation of OSNs only within the targeted

glomerulus while avoiding spurious excitation of passing-by OSN axons that terminate in neighboring glomeruli. To assess the efficacy of our approach, we set the photo-stimulation and multiphoton activity readout planes to overlap axially in the glomerular layer, such as to stimulate the OSNs and image the resultant postsynaptic glomerular response in the dendrites of MT cells. Photo-stimulation induced rapid and reliable changes in fluorescence (**Fig**. **4**). For each photo-stimulation mask (**Figs**. **4b-e**, **S3b**), we constructed a two-dimensional light activation map (2DLAM) at sub-glomerular resolution[36] (e.g. 40 x 40 grid of 7.2 µm pixels, Methods). To ensure we operated in a regime of specific glomerular activation, we successively lowered the light intensity until no light-triggered activity was observed in neighboring glomeruli (15-to-2 mW / mm^2, 122 glomeruli, 21 FOVs, 7 mice, **Figs**. **4f**, **S3c**). Across mice, we identified a range of intensities that on average resulted in specific and reliable activation of targeted glomeruli and negligible activation of adjacent glomeruli (**Fig**. **4f**).

Next, we axially decoupled the photo-stimulation and imaging z-planes to monitor light-triggered responses in the cell bodies of the corresponding *daughter* M/T cells (receiving excitatory input from the targeted glomeruli, and 100-270 µm deep from surface), while still photo-stimulating individual glomeruli on the bulb surface (**Figs**. **5a-e**, **S4a-f**). Photo-stimulation of individual glomeruli evoked robust excitatory responses in ~19 % of the cells (162/856). The majority of these responsive cells (141/162) were activated by only one unique glomerulus that we ascribed as their corresponding parent glomerulus. A small proportion of cells were activated by more than one glomerulus and excluded from were further analysis (21/162 cells, **Fig**. **5b** *iii*, cell 30). By comparing the identity of parent glomeruli across the imaged M/T cells, we identified cohorts of *sisters* as the cells that were activated by the same parent glomerulus.

Figure 5

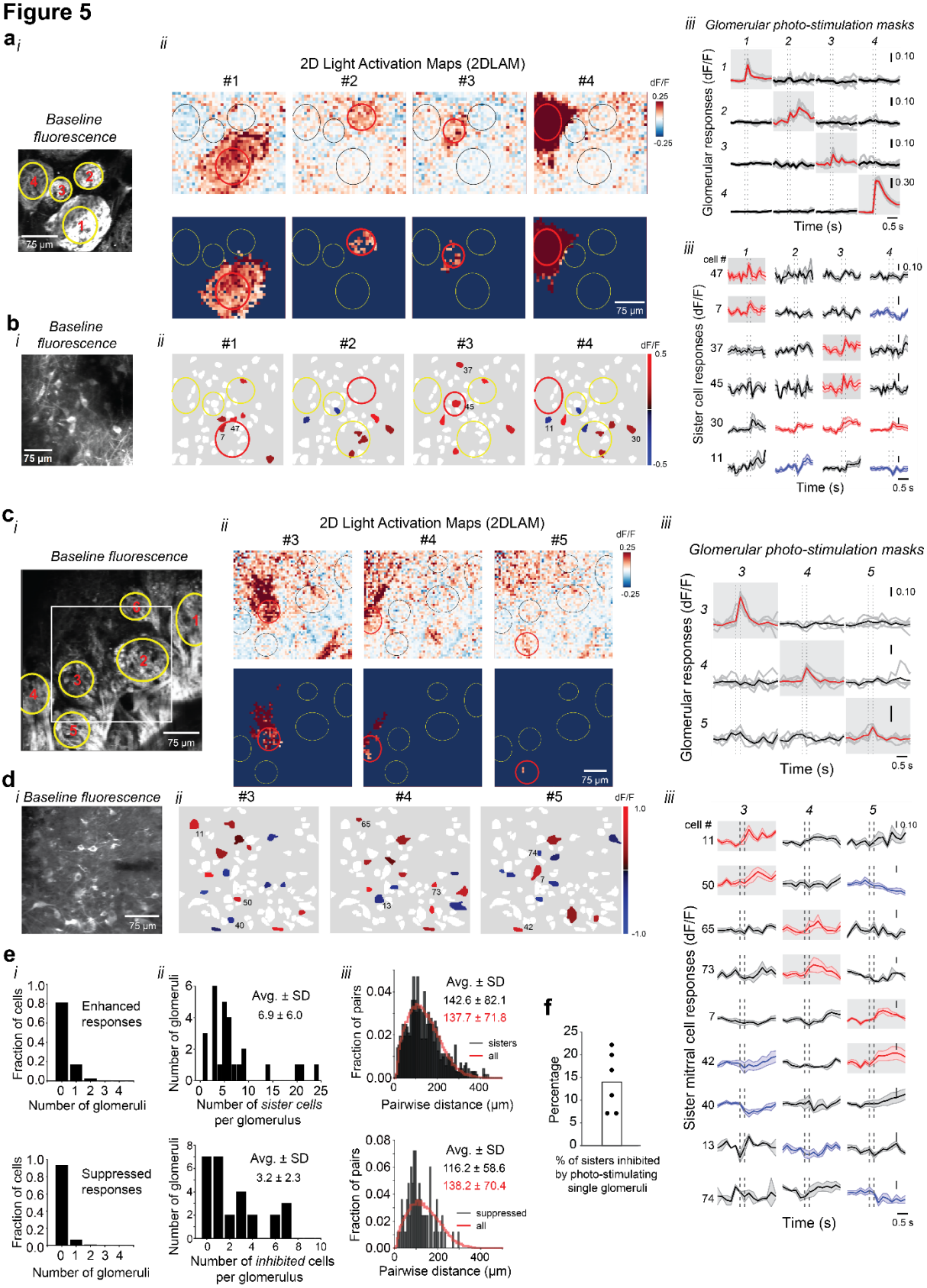

Figure 5. Identifying sister mitral and tufted cells via axially decoupled glomerular stimulation and two photon fluorescence imaging. ***(a-b)*** *anaesthetized,* ***(c-d)*** *awake.* ***(a)*** *(i) Resting glomerular fluorescence (ReaChR-mCitrine and GCaMP6s); (ii) Fluorescence changes (raw, Top and significant pixels glomerular 2DLAMs, Bottom) evoked by photo-stimulation of four target glomeruli (7.5 mW/mm^2); (iii) Response matrix of fluorescence change traces (individual repeats in gray, and mean signal as thicker lines) corresponding to four glomerular regions of interest versus the four corresponding (matching) glomerular light masks projected on the OB surface. Red shaded areas mark responses of the targeted glomerulus in a given trial. (**b**) (i) Resting fluorescence (GCaMP6s) of mitral cell bodies at the same x-y coordinates, 210 µm below the glomerular field of view in (**a**); (ii) Significant cell body responses evoked by photo-stimulation of the four target glomeruli (**a**, 7.5 mW/mm^2); (iii) Average fluorescence response traces corresponding to six example mitral cells in each heat map, whose positions are indicated by numbers in (ii); shaded area marks SEM. Two example pairs of sister cells (47, 7 with respect to parent glomerulus #1; and 37, 45 with respect to parent glomerulus #3) are shown. Note that cell #30 is non-specifically responding to photo-stimulation of multiple glomeruli (#2,#3,#4). In addition, glomerular photo-stimulation triggered sparse suppressed responses (e.g. cells 7,11) intermingled with the sister cells.* ***(c)*** *(i-iii) Same as (**a**) for an example awake experiment: photo-stimulation of three target glomeruli (2.5 mW/mm^2; 50 ms light on/trial); (iii) Response matrix of fluorescence change traces (individual repeats in gray, and mean signal as thicker lines) corresponding to three glomerular regions of interest (#3,#4,#5) versus the three (matching) glomerular light masks projected on the OB surface. Stimulation of glomeruli #1 and #2 resulted in non-specific responses. (**d**) (i-iii) same as (**b**) for an example awake experiment sampling mitral cell bodies at the same x-y coordinates, 190 µm below the glomerular field of view shown in (**c**); (ii) Significant cell body responses evoked by photo-stimulation of three target glomeruli (**c**,ii); (iii) Average fluorescence time traces corresponding to nine example mitral cells in each heat map, whose positions are indicated by numbers in (ii). Three example pairs of sister cells (11, 50 with respect to parent glomerulus #3; 65, 73 with respect to parent glomerulus #4; and 7 and 42 with respect to parent glomerulus #5) are shown. Glomerular photo-stimulation also triggered spatially distributed suppressed responses (e.g. cells 13, 40, 42, 50, 73, 74), denser than in anaesthetized mice.* ***(e)*** *(i) (Top) Specificity of enhanced responding mitral and tufted cells as a function of the targeted glomerulus (N = 6 mice; 27 responsive and specific glomeruli / 46 photo-stimulated target glomeruli; 856 mitral & tufted cells). Note that most cells were non-responsive, or responded specifically to the photo-stimulation of the target glomerulus (13 % of cells had off-target responses to more than one glomerulus; see* ***Fig. S4a****, Methods); (Bottom) Same for suppressed responses. (ii) (Top) Number of observed sister cells (enhanced responses) per glomerulus photo-stimulation across fields of view (Left; 6.9 ± 6.0, N = 27 FOVs); (Bottom) Number of cells whose baseline fluorescence was suppressed upon photo-stimulation of the same glomeruli (Right; 3.2 ± 2.3, N = 20 FOVs); (iii) (Top) Pairwise distance between sister cells vs. between any cells in the field of view (142.6 ± 82.1 µm vs. 137.7 ± 71.8 µm; 725 vs. 29,850 pairs). (Bottom) Pairwise distance between suppressed cells vs. any cells in the field of view (116.2 ± 58.6 µm vs. 138.2 ± 70.4 µm, 83 vs. 19,607 pairs). Unless specified Avg. ± SD values are shown.* ***(f)*** *Photo-stimulation of individual (non-parent) glomeruli triggered inhibitory responses in only a small subset of the sister cells of a given identified cohort (Avg. ± SEM, 14.0 ± 2.7 %, N=6).*

On average, across experiments (10 FOVs, 6 mice, 27/46 response evoking glomeruli) we identified 6.9 ± 6.0 (Avg. ± SD) *sister* mitral and tufted cells per glomerulus (4 SD response threshold, see Methods). Consistent with previous literature[36,56,58,63,83], *sister* cells were spread across the field of view and spatially intermingled with cells receiving inputs from other glomeruli (*non-sisters*) (Avg. ± SD: 142.6 ± 82.1 µm pairwise distance between *sister* cells vs. 137.7 ± 71.8 µm between any cells in the FOV). Note that the statistics reported here underestimate the number of *sister* cells per glomerulus[58] simply because of the limited number of different depths (z-optical planes) and the size of fields of view sampled for this experiment.

In addition to light-triggered excitatory responses, we also observed sparse light-induced suppression of the baseline fluorescence in 3.2 ± 2.3 cells per glomerulus. These suppressed cells were intermingled with the identified *sister* cells, and peppered the fields of view (3 SD response-to-baseline signal threshold; 116.2 ± 58.6 µm pairwise distance of suppressed cells vs. 138.2 ± 70.4 µm between any cells in the field). We interpret the observed decrease in M/T resting fluorescence as the suppression of respiration-locked baseline firing patterns[84–86] due to lateral inhibition from the photo-stimulated glomeruli acting via local bulbar circuits. Interestingly, we could also observe such light-triggered suppression for a subset of the *sister* cell cohorts (6/27 *sister* cell cohorts) identified via *ADePT*. This allowed us to assess whether *sister* cells receive lateral inhibitory inputs from the same or different glomeruli. Photo-stimulation of individual, *non-parent* glomeruli inhibited a small fraction of *sisters* within a cohort (1-2 *sisters* per cohort; Avg. ± SEM, 14.0 ± 2.7 %, N=6, **Fig. 5f**, Methods). In rare instances, where we observed inhibition in 2 or more *sister* cells, we found that different *sister* cells were suppressed by photo-stimulation of different individual glomeruli (**Fig. S4f**). These data indicate that indeed *sister* cells, while sharing excitatory drive from the same parent glomerulus, receive sparse inhibitory inputs from different

sets of non-parent glomeruli. This is in agreement with previous reports of differences in *sister* cells spike-timing across the respiration cycle[36,55,78]. While further investigation is needed to understand the logic of these lateral inhibitory interactions, these experiments show that *ADePT* is well-suited for direct mapping of excitatory/inhibitory connections in layered neuronal circuits.

Application 2: Assessing the spatial heterogeneity of long-range olfactory bulb inhibition

Next, we used *ADePT* to assess the spatial heterogeneity in the impact of GABAergic/dopaminergic (DAT+ cells, historically known as superficial short axon cells), a class of long-range inhibitory interneurons in the glomerular layer, on the activity of mitral and tufted cells. DAT+ neurons integrate excitatory inputs within individual glomeruli and establish chemical and electrical synapses with other interneurons and mitral/tufted cells within other glomeruli located as far as 1.5 mm away[43,66,67,71–73,87]. Given these long-range processes, DAT+ cells are thought to re-distribute focal glomerular odor inputs and convey long-range signals across the glomerular layer. Work from several groups including ours[42,43,66–73,88] suggested that DAT+ neurons enable olfactory circuits to negotiate wide variations in odor concentration by implementing a form of global gain-control (divisive normalization)[42,43,68,89]. However, it remains unclear whether DAT+ cells broadcast inhibitory inputs uniformly within a local neighborhood or act selectively on particular cells that share specific features such as similarity in odor tuning[43,67,88,90]. This is due to previous technical constraints in controlling the activity of DAT+ cells in conjunction with simultaneous imaging of activity in the mitral and tufted cells. We used *ADePT* to photo-stimulate DAT+ cells associated with individual glomeruli while monitoring their impact on either the spontaneous or odor-evoked responses of mitral/tufted cells.

We first tested the specificity of targeting DAT+ interneurons across glomerular regions of interest using mice co-expressing both an opsin (ChR2-mCherry[91]) and a calcium indicator (GCaMP6f[80]) in the DAT+ cells (**Fig. S5a**). We selected individual adjacent glomeruli for photo-activation, triggering and reading out DAT+ cell activity in the same optical z-plane. Through these experiments, we identified a range of light intensities across which the stimulus-responsive area remained confined to the glomerulus targeted for photo-stimulation (**Figs. S5b-e**, Methods).

To assess the impact of glomerular DAT+ interneurons on the activity of mitral and tufted cells, we used mice expressing an excitatory opsin in DAT+ cells and the calcium indicator GCAMP6f in mitral/tufted cells (DAT-Cre x Thy1GCaMP6f[80,92] mice injected retro-orbitally with ChrimsonR-tdtomato AAV-PHP.eB:Syn-FLEX-rc[ChrimsonR-tdtomato][93,94], **Fig.S6a**, Methods). We optogenetically activated DAT+ neurons and monitored the ensuing tufted and mitral cell responses 120-275 µm below the photo-stimulated glomeruli (**Fig. 6**). On average, glomerular DAT+ photo-stimulation targeted to *single* glomeruli resulted in dense, but heterogeneous suppression of the *baseline fluorescence* in mitral cells across the field of view (fraction of mitral cells modulated in example field of view: 0.40 ± 0.19; 200 x 200 µm, 294 cell-mask pairs, **Figs. 6a-d**, **S6b-d**). Stimulation of different DAT+ glomerular masks resulted in ensemble mitral cell responses that were significantly different from each other, but more correlated than the average pairwise responses for controls where cell identities were shuffled (**Fig. 6e**; 0.42 ± 0.23 vs. 0.29 ± 0.19, $p<0.001$, Wilcoxon signed-rank test) or across odors (**Fig. 6e**; 0.42 ± 0.23 vs. 0.25 ± 0.35, $p<0.001$, Wilcoxon signed-rank test). As reference, we also calculated a 'self' correlation to assess the variability of photo-stimulation responses to the *same* DAT+ glomerular mask across trials (Methods). Responses of mitral cell ensembles across different DAT+ masks were substantially

lower than the 'self' control (0.42 ± 0.23 vs. 0.81 ± 0.14, p<0.001, Wilcoxon signed-rank test, **Figs. S6b**), demonstrating significant impact of DAT+ neurons on OB outputs.

Figure 6

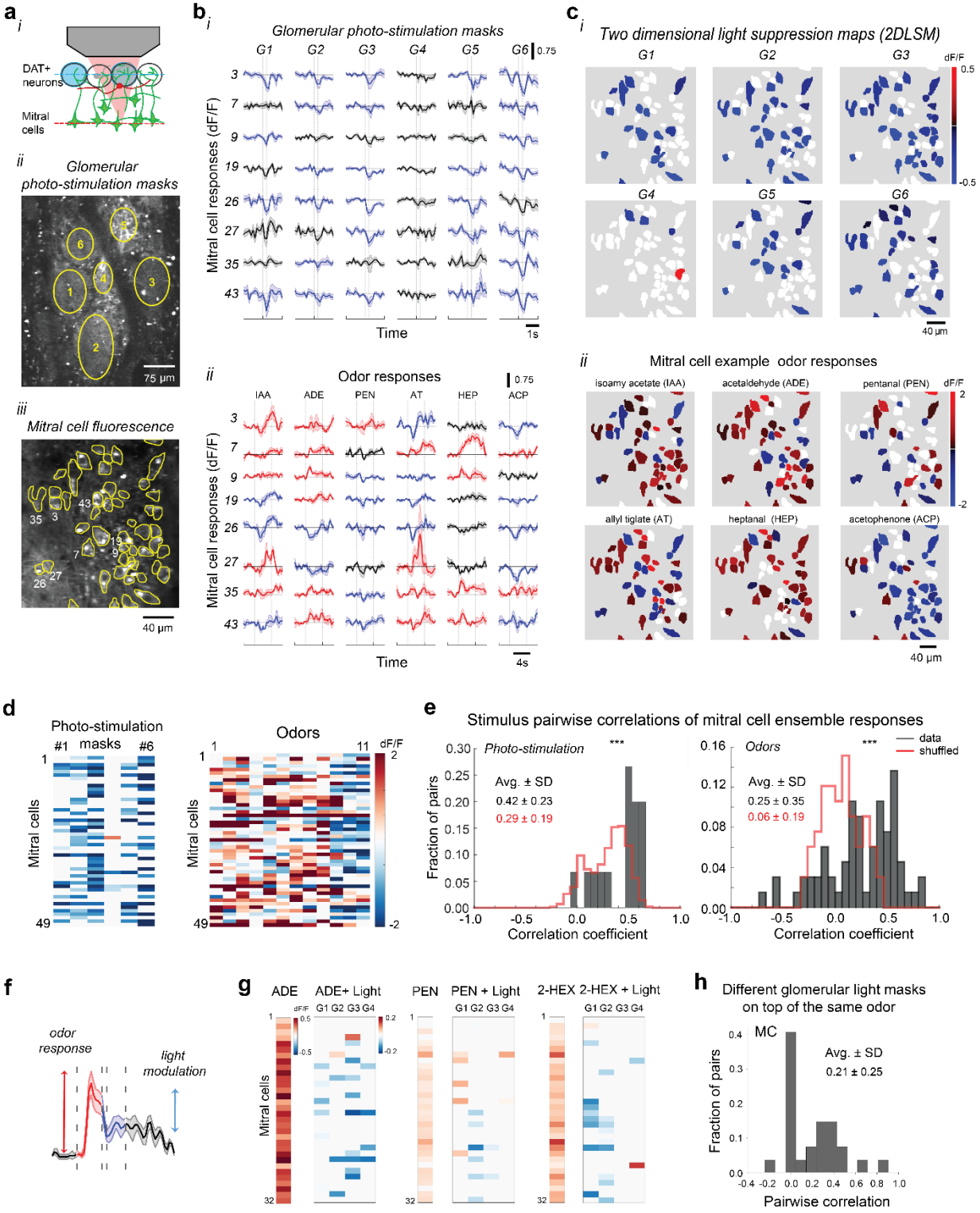

Figure 6. Glomerular photo-activation of DAT+ interneurons triggers dense, but spatial heterogeneous inhibition of mitral and tufted cell activity. (a) *(i) Cartoon schematics: photo-stimulation of opsin expressing DAT+ cells while monitoring mitral cell activity (GCaMP6f) by axial decoupling of the photo-stimulation and imaging planes (awake). (ii) Example glomerular field of stimulation; mice express GCaMP6f in mitral and tufted cell glomerular dendritic tufts and ChrimsonR-tdtomato in DAT+ cells (not shown). (iii) Example field of view of mitral cells imaged while photo-stimulating DAT+ cells (200 ms, 7.5 mW/mm^2) in the glomerular layer.* ***(b)*** *(i) (Top) Dense, but heterogeneous inhibition of baseline fluorescence in mitral cells across the field of view evoked by photo-stimulation of DAT+ cells across six target glomerular light masks (G1-G6); (Bottom) Odor responses of the same example mitral cells to six odors (isoamyl acetate, IAA; acetaldehyde, ADE; valeraldehyde, PEN; allyl tiglate, AT; heptanal, HEP; acetophenone, ACP).* ***(c)*** *(i) (Top) Fluorescence changes (two dimensional light suppression maps) in mitral cells evoked by photo-stimulation of DAT+ cells across six individual glomerular light masks (G1-G6); (Bottom) Diversity of same mitral cell responses to six example odors (**b**); each cell in the field of view is displayed on a blue-to-read color scale indicating its response amplitude to light/odor stimulation; non-significant responses were thresholded to white (Methods).* ***(d)*** *Peak fluorescence changes (dF/F) of same mitral cells (49) across the field of view in response to glomerular DAT+ cells photo-stimulation (Left) and to a panel of eleven odors (Right).* ***(e)*** *(Left) Correlation distribution of mitral cell ensemble responses across different pairs of DAT+ cell glomerular photo-stimulation masks (G1-G6). (Right) Same across pairs of odors in the panel (1-11). Shuffled mitral cell index control distributions are shown in red; 'self' control (see **Fig. S6b-d**).* ***(f-h)*** *anaesthetized, also see **Fig. S7a-f**;* ***(f)*** *Fluorescence change (dF/F) elicited by odor presentation in one example tufted cell, and its subsequent modulation by projecting of a glomerular light mask to optogenetically augment DAT+ cell activity (500 ms, 10mW/mm^2; 2s from odor onset).* ***(g)*** *Mitral cell peak odor responses (ADE, PEN, 2-HEX) and their modulation by 4 glomerular DAT+ cell glomerular light masks in an example field of view (**Fig. S7**).* ***(h)*** *Stimulus response pairwise correlations of mitral cell ensembles: distribution of pairwise correlations for different glomerular DAT+ cells photo-stimulation masks imposed on top of the same odor aggregated across the three odors in (**g**) (0.21 ± 0.25; 27 pairs, 2 FOVs, 39 MC cells).*

Stimulation of DAT+ neurons results predominantly in the suppression of mitral and tufted cells from their baseline activity. To boost the baseline M/T cell fluorescence and better characterize the impact of DAT+ neurons, we presented odors (4s) in conjunction with DAT+ cell photo-activation in the middle of the odor presentation period. Similar to the experiments described above (**Figs. 6a-e**), stimulating DAT+ cells *across different glomeruli* during odor presentation also resulted overall in differential suppression of the OB outputs (**Figs. 6f-h**, **S7a-f**, TC: 0.44 ± 0.33; MC: 0.21±0.25; pairwise correlation, $p<0.001$, Wilcoxon signed-rank test; modulation by light on top of odor: 78.0 % unmodulated, 18.2% suppressed vs. 3.8% enhanced MC-odor-pairs; N=2,214

pairs; and 54% unmodulated, 42.6% suppressed vs. 3.4% enhanced TC-odor pairs, N = 945 pairs). Thus, we find that the impact of DAT+ cells on the OB output is dense, but locally heterogeneous with different cells exhibiting diverse sensitivities to DAT+ inhibition originating from a given glomerulus (**Fig**. **6**). Further investigation will determine whether DAT+ cell action shapes the MC and TC cell odor responses in a systematic manner as a function of similarity in their odor responses.

In summary, we show that *ADePT* can be flexibly combined with genetic strategies and/or sensory stimuli to probe the contribution of both excitatory and inhibitory neuronal types in shaping the output of optically accessible neuronal circuits.

Discussion

We demonstrate a readily implementable method (*ADePT*) for optical control and recording of activity in three-dimensional neural structures by decoupling the focal planes for optogenetic patterned stimulation and multiphoton imaging. When referenced to other comparable techniques[8,9,13,20–22,29–33], *ADePT* enables us to control neuronal activity across a wide field of view, does not suffer from aberrated imaging, and is easy to implement. We confirmed that we were able to maintain precise spatial control over a range of activation powers and demonstrated the usefulness of the system by mapping *both excitatory and inhibitory* functional connectivity in the mammalian olfactory bulb.

ADePT allows arbitrary axial shifting of 2D photo-stimulation light patterns of choice relative to the focal plane of the imaging objective by translating a motorized diffuser along the photo-

stimulation optical path (**Fig**. **1**). As a function of its angular divergence, the choice of the diffuser determines the degree of axial confinement of the photo-stimulation pattern, enabling optical sectioning in the widefield illumination configuration, and also increasing homogeneity in the photo-stimulation patterns (**Figs**. **2**,**3**). The larger the angular divergence of the diffuser, the tighter the axial extent of the pattern, which comes at the expense of excitation light loss. In our implementation, we controlled glomerular activity optogenetically over a 1.5 x 1.2 mm field of stimulation with ~ 20 µm lateral and ~ 40 µm axial resolution. Different magnification choices in the photo-stimulation path, however, can be used to customize the extent of the field of stimulation with inherent resolution trade-offs. In its current implementation, *ADePT* does not afford the resolution to optogenetically target individual cells, but is effective in controlling the activity of larger input units (e.g. single olfactory glomeruli, whisker barrels) in neural circuits of interest, while monitoring their impact across different cell types at cellular resolution via multiphoton imaging of changes in activity. Furthermore, different choices of the diffuser enable tighter axial resolution at the expense of photo-stimulation light loss (grit ground diffuser vs. holographic diffusers, **Fig**. **2**). While achieving axial-confinement of extended 2D photo-stimulation patterns (**Fig**. **2**), *ADePT* is effective for optical control of activity largely in the superficial brain layers, since it is constrained by light scattering-related degradation (**Fig**. **S2**).

In proof-of-principle experiments, we used *ADePT* to investigate the functional connectivity of olfactory bulb circuits in the mouse. We controlled optogenetically the activity of select excitatory and inhibitory cell types in the input layer (OSNs vs. GABAergic/dopaminergic DAT+ interneurons) at *sub-glomerular* resolution, while monitoring their impact on the responses of the principal neurons (mitral and tufted cells). By targeting optically addressable glomeruli (**Figs**. **4**,**5**),

437 we identified multiple cohorts of daughter *sister* mitral and tufted cells driven by *parent* glomeruli
438 and revealed sparseness and differential action in the olfactory bulb inhibitory lateral interactions
439 (**Fig. 5**). Our approach further enables discriminating between different inhibitory inter-glomerular
440 connectivity schemas (e.g. uniform vs. heterogeneous) implemented by different cell populations
441 (e.g. GABAergic/dopaminergic DAT+ interneurons)[43,67,88], and testing hypotheses on how
442 connectivity relates to the similarity in odor response tuning[67,90]. We found that DAT+ cells
443 associated with different glomeruli mediate dense, but heterogeneous (non-uniform) suppression
444 of MC and TC baseline and odor responses (**Fig. 6**).
445
446 Compared to previous work on mapping individual glomerular outputs[36,55], *ADePT* affords one-
447 to-two orders of magnitude higher throughput and cell type specificity in the activity readout.
448 Identifying multiple cohorts of *sister* cells is key for determining the specificity of inhibitory inputs
449 that principal OB neurons integrate to compute relevant stimulus features. As previously
450 proposed[36,55,56], we found that *sister* cells, driven by the same *parent* glomerulus, receive
451 differential inhibitory input from other glomeruli with implications for odor coding. As such, many
452 more output information channels may leave the bulb than then number of input sensory afferent
453 types. Increasing the number of *sister cell cohorts* mapped to their *parent* glomeruli, and
454 systematic photo-stimulating spatial-temporal combinations of multiple (*non-parent*) glomeruli
455 will enable further testing hypotheses on how inhibitory connectivity relates, for example, to the
456 degree of similarity in the odor responses of the corresponding input glomeruli. In recent
457 sequencing-based single-cell projection mapping, we identified structure in the projections of
458 individual mitral cells at different locations along the A-P axis of the piriform cortex with respect
459 to their co-projections to extra-piriform target regions[95,96]. By combining functional mapping and

anatomical DNA barcoding projection mapping approaches, future work will determine whether the *sister* outputs of individual glomeruli segregate into parallel functional streams that may support different computations related to perception versus valence versus action[96] during odor-guided behaviors.

More broadly, simultaneous patterned photo-stimulation and multiphoton imaging in different axial planes enables mapping functional connectivity not only in the olfactory bulb, but can be implemented between any optically accessible brain regions (across layers) including the neocortex. For example, *ADePT* is well positioned for mapping functional connectivity in the barrel cortex within and across barrels[34,97], as well as bidirectional interactions between cortical visual areas (V1 vs. PM, AL, etc.)[98,99], visuomotor (M2-V1)[100–102] or audiomotor circuits (M2-A1)[103,104], etc. Given its relative simplicity, cost-effectiveness, and ease-of-use, compared to other axially decoupling optical imaging and photo-stimulation strategies, *ADePT* is readily applicable for investigating the logic of neural connectivity.

Acknowledgements: The authors acknowledge R. Eifert and D. Cowan for technical support. This work was supported by NIH 5R01DC012853-05, NSF IOS-1656830 to D.F.A. and Beckman Institute CLOVER (CLARITY, Optogenetics, and Vector Engineering Research) to V.G.

Data and code availability: All data matrices included in the analyses presented here representing mitral/tufted and GABAergic/dopaminergic DAT+ interneuron GCaMP responses triggered by

odor and optogenetic light stimuli, as well as the code used for the instrument control and analysis are available upon request.

Declaration of interests: The authors declare no competing interests.

Authors contributions: conceptualization, investigation, methodology, formal analysis, visualization, software, data curation and writing, M.K., F.A.; methodology, formal analyses, visualization, data curation, validation, software, S.K.K., S.S.T; methodology, visualization, validation, D.E.H., W.G.B., P.S.V., H.C, M.B.D.; reagents development, Z.Q., V.G.; conceptualization, methodology, formal analysis, visualization, and writing, A.B.; conceptualization, methodology, formal analysis, visualization, software and writing, P.G.; conceptualization, methodology, investigation, methodology, writing, supervision, project administration, and funding acquisition, D.F.A.

Methods

Combined two-photon imaging and photo-stimulation microscope: For *two photon imaging* (**Fig. 1b**), the output from a Ti:Sapphire laser (Coherent Chameleon Ultra II) was magnified by a 1.5x beam expander (L1, L2, focal lengths, FL: 40, 60 mm), then reflected off two mirrors (10D20ER.4, Newport) and a periscope onto a galvanometric mirror scanning system (GM, 6215HB, Cambridge Technologies). The semi-stable stationary point between the GM was expanded and imaged to fill the back aperture of the microscope objective by a telescope (L3, AC300-050-B, L4, AC508-300-B, FL 50, 300 mm, Thorlabs). The objective and microscope stage

were mounted on motorized linear translators (x-y stage: 462-XY-M; z-stage: CMA-25CCCL, Newport) connected to a three-axis motion controller (Newport ESP301). Fluorescence light from the sample was collected by the objective, then reflected by a dichroic mirror (DM1, 680dcxr, 50 mm diameter, Chroma) placed atop of the imaging objective (Olympus 20x 1.00 NA XLUMPlanFLN) and a second short-pass dichroic mirror (DM2, 505 nm, FF505-SDi01-50.8-D, 50 mm diameter, Semrock) towards a GaAsP PMT (H11526-20-NF, Hamamatsu) for green or red fluorescent detection (sliding holder, LCFH2 green, FF03-525/50-25 and red, FF01-607/70-25 emission filters, Semrock). The back aperture of the microscope objective was imaged into the PMT aperture by a telescope (L5/L6, FL: 100/32 mm; L5 – LA4545-A (UV fused silica); L6 - AL4532-A, Thorlabs). The current output of the PMT was transformed to voltage, amplified (SR570, Stanford Instruments) and digitized using a data acquisition board (NI-PCI-6115, National Instruments). The same board was also used to generate signals for controlling the galvano-metric mirrors. By rotating DM2 by 90° on a custom holder (CSHL, Machine Shop), light was directed either to the PMT or to a CCD camera (Vosskuhler 1300-QF, **Fig**. **1**). The image of the sample was further minified by a telescope (L7/L8, focal lengths: 100/40 mm) and captured on the CCD chip (CCD 1), allowing for a larger field of view of approximately 1,500 x 1,200 µm. Additional short pass filters (FF01-750/SP-50, 50 mm diameter, Semrock) were used in front of light detectors (CCD and PMTs) to block stray light from the infrared multiphoton excitation laser. For *patterned photo-stimulation*, the beam from a 488-nm laser (Coherent Sapphire 488, 200mW) was magnified using a beam expander (L12/L11, FL: 30/300 mm) and reflected by a mirror and a periscope (RS99, Thorlabs) onto the surface of a DMD chip (DMD 0.7" XGA VIS, Vialux GmbH, 1024 x 768 pixels, 13.68 µm micro-mirror pitch). The DMD chip was controlled using a Vialux DLP-Discovery 4100 board and the corresponding application programming interface (Vialux

GmbH). To obtain direct access to the chip, we removed the projecting lens and prism installed in front of the DMD by the manufacturer. The steep angle of incidence of the photo-stimulation beam onto the DMD was carefully tuned to ensure maximal diffraction efficiency. The patterned beam reflected off the DMD was further magnified by a L10/L9 telescope (FL 100/200 mm), and coupled into the microscope by DM1. An iris (SM2D25, Thorlabs) was placed at the front focal plane of L10 to block the higher diffraction order replicas of the DMD-generated spatial pattern. The photo-stimulation pattern was further projected into the sample by the tube lens (L5, FL 100 mm) and the principal objective (Olympus 20x 1.00 NA XLUMPlanFLN).

Diffuser: A diffuser was used to axially confine the photo-stimulation pattern. The diffuser was mounted on a translational stage (Newport, 433-series, #BZA647202) connected to a stepper motor. The motor was controlled using an open source Arduino-based system[105]. In the home position (imaging and photo-stimulation planes superimposed), the diffuser sits at the focal plane of the tube lens L5. Three different round diffusers (25 mm diameter) were tested, as detailed in the text: two holographic diffusers with 5° and 10° divergence angle (5° - #55-849, 10° - #48-506, Edmund Optics), and a grit ground glass diffuser (#38-786, Edmund Optics). Two fast shutters (Uniblitz VS14) were placed in front of the PMT and the blue photo-stimulation laser respectively, and operated in anti-phase so that only one shutter was open at a time such as to alternate between periods of photo-stimulation and photon collection.

Excitation power control and lenses: The excitation two photon laser power was controlled by a Pockels cell (Conoptics 350-80 BK) placed in the imaging path. An additional filter (775 nm long pass, 25 mm diameter, #86-069, Edmund Optics) was added to the excitation path to block a

551 residual red component from the Ti:Sapphire laser, that would otherwise saturate the red PMT.
552 When required, additional neutral density filters (Thorlabs, NDK01) ranging from ND 0.2 to ND
553 2.0 were added to the photo-stimulation path to further reduce the power. All lenses (Thorlabs)
554 had anti-reflective coating for either infrared (imaging path) or visible (photo-stimulation and
555 detection paths) light. A UV fused silica lens was used instead of the more common N-BK7 lenses
556 in position L5 (LA4545-A) to avoid spurious phosphorescence signals following illumination with
557 intense blue light pulses (see *Phosphorescence Artifacts*).
558
559 **Auxiliary microscope:** An auxiliary microscope was used during characterization experiments,
560 as described in *Lutz et al. (2008)*[6]. We placed a secondary objective, tube lens and green emission
561 filter (HQ510DCLP, Chroma) below the main imaging objective to image the focal plane of the
562 main objective onto a CCD camera (Vosskuhler 1300-QF, **Fig. 3a**). Depending on the experiment,
563 different objectives (Olympus 4X, 0.13 NA UPlanFlN or Olympus 20X, 0.50 NA UPlanFlN) were
564 used in combination with a 150 mm focal length tube lens to obtain either a minified image of the
565 entire field of photo-stimulation or a higher resolution image of a smaller field. The microscope
566 framework was constructed with a Thorlabs 2" cage system. The secondary objective was held
567 either by a kinematic mount for fine tilt adjustment (KC2-T, Thorlabs), or by a laterally-
568 translatable platform. The photo-stimulation patterns were imaged onto a coverslip spin-coated
569 with a thin (~1 µm) rhodamine B layer (courtesy of V. Emiliani, Paris Descartes University).
570
571 **Calibrating decoupling of photo-stimulation and imaging planes:** We used the auxiliary
572 microscope to calibrate the decoupling of photo-stimulation and imaging planes (**Fig. 3a**). Initially,
573 the diffuser was positioned at a plane conjugated to the focal plane of the principal and auxiliary

objectives, and the photo-stimulation pattern was in focus on the coverslip, appearing sharp both on the principal (primary) and the auxiliary (secondary) CCD cameras (**Fig**. **3a**, *Left*). The principal objective was then moved closer to the coverslip to simulate shifting the imaging plane to deeper layers in a biological preparation. At this point, the photo-stimulation pattern was still imaged (projected into sharp focus) on the focal plane of the principal microscope objective (now below the coverslip), and no longer in focus on the secondary CCD camera. To move the photo-stimulation pattern back to the initial position, we moved the diffuser away from the tube lens (L5) until the projected pattern was again in focus on the fluorescent coverslip and on the secondary CCD camera (**Fig**. **3a**, *Right*). Using this strategy, we iteratively constructed an empirical calibration curve that relates the diffuser displacement to the position of the photo-stimulation plane in the sample with respect to the focal/image plane of the principal objective (**Fig. 3b**).

Relating movement of the objective to the adjusting displacement of the diffuser: Within the thin lens approximation framework, let u be the distance between the objective (O) and the image of the projected light pattern, s_i+s_o the distance between the objective and the tube lens (L5), v the distance from the diffuser to the tube lens, and f_1 and f_2 the focal lengths of the objective and the tube lens.

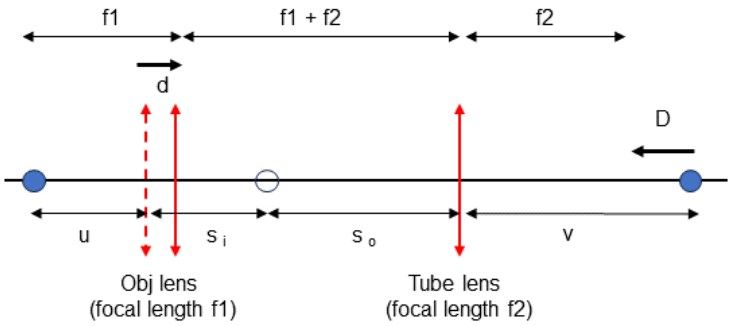

How does the displacement of the objective (d) relate to the displacement of the diffuser (D) needed to bring the projected pattern in focus in the desired z-plane in the sample, as a function of

magnification (M) of the system given by the ratio of focal lengths of the tube lens and objective lens ($M=f_2/f_1$)?

$$v = \frac{u * f}{u - f} \quad \textbf{Eq. 1}$$

Calculating image distance ($u = f1 - d$) for the objective lens (O), when d is small:

$$s_i = \frac{(f1 - d)) * f1}{(f1 - d - f1)}$$

$$s_i = -\frac{(f1 - d) * f1}{d} \quad \textbf{Eq. 2}$$

For the tube lens, the object distance is: $s_o = (f1 + f2 + d) - s_i$

Replacing s_i from *Eq. 2*:

$$s_o = (f1 + f2 + d) + \frac{(f1 - d) * f1}{d}$$

Since *d* is small, ignoring higher order terms of *d*, we obtain:

$$s_o = \frac{f1^2 + f2 * d}{d} \quad \textbf{Eq. 3}$$

For the tube lens, image distance (v) is given by:

$$v = f2 + D = \frac{s_o * f2}{s_o - f2}$$

Solving for *D*:

$$D = \frac{s_o * f2}{s_o - f2} - f2$$

$$D = \frac{f2^2}{s_o - f2} \quad \textbf{Eq. 4}$$

Replacing s_o and solving for D:

$$D = \left(\frac{f2}{f1}\right)^2 * d \quad \textbf{Eq. 5}$$

Therefore, we find that the axial displacement of the photo-stimulation plane at the sample (d) is linearly proportional to the translation of the diffuser in the optical path (D).

Photo-stimulation and imaging calibrations

DMD-chip to CCD-chip to multiphoton image registration: To photo-stimulate specific locations in the sample, we determined where a given *pixel on the DMD* falls on the *specimen* using the primary camera (CCD1) as a reference. After registering pixels on the DMD-chip to CCD1 chip pixels, a point-to-point correspondence between the DMD-chip and the focal plane of the principal objective was obtained. Further, the auxiliary microscope was used to map the correspondence between pixels on the *DMD* and the *specimen* in z-planes out of the focal plane of the principal objective. To map pixels in the *two photon field of view* to the *DMD*, we also used CCD1 as intermediary reference. Within this frame of reference, we targeted ROIs that were axially (z) displaced from the principal objective focal plane, and imaged either using the primary CCD camera or the two photon microscope. Pixels of the DMD-chip were mapped onto pixels of CCD1 by projecting a series of light spots generated from known DMD locations. Routinely, we placed 20 µm sized spots in a 4 x 5 grid spanning the field of stimulation. After recording the position of all these fiduciary light spots, we computed the 3 x 3 matrix $\mathbf{T} = \mathbf{D}\mathbf{C}^{\mathbf{T}}(\mathbf{C}\mathbf{C}^{\mathbf{T}})^{-1}$, where **C** and **D** are N x 2 matrices whose rows contain the light spot coordinates on the CCD1 and DMD chips respectively. The matrix **T**, when left-multiplied with CCD1 chip coordinates, transforms CCD1 coordinates into DMD-chip coordinates. To verify this procedure, a high-density sample with 15 µm fluorescent latex microbeads was imaged using first the widefield fluorescence path (CCD1), and subsequently the two photon microscope. Individual microbeads were matched between the acquired images manually (*cpselect* tool in the MATLAB image processing toolbox). We obtained

a look-up table of two photon / CCD1 images point pairs. Further, by minimizing the sum of squared errors, we calculated the corresponding transform matrix that maps two photon image pixels onto CCD1 image pixels. The absolute position of a particular location in a two photon image is dependent on both the field of view and the resolution settings (number of pixels) of the image. Several FOV and pixel resolution settings were chosen for registration, and further used accordingly when targeting ROIs within a two photon reference image. Post-registration, we verified that the targeting of the DMD-chip generated patterns was precise. The control software reproduced the desired target light spots with high accuracy within the field of stimulation, using only the two photon image or only the CCD1 image as guide; error between projected centroids light spots vs. fluorescence microbeads was less than 5 µm, **Figs**. **1d**, **S1d**.

Correcting the field of photo-stimulation power inhomogeneity: Due to the Gaussian intensity profile of the blue laser beam illuminating the DMD chip, the power towards the borders of the field of photo-stimulation is lower than in the center. To correct for this inhomogeneity, and ensure flatness of photo-stimulation across the field, we calculated a power distribution map (PDM) across the field of stimulation, obtained by sequentially projecting 25 µm spots in an 11 x 11 grid pattern covering 121 pixel coordinates across the DMD-chip, and by linearly interpolating such as to estimate the power at the remaining positions. We projected the spot pattern on the DMD chip and placed a power sensor (Thorlabs, 50mW, S120B) under the primary objective with the pattern in focus. For simple patterns, such as spatially-localized single spots, the laser power can be adjusted accordingly using the PDM look-up table to compensate for power loss at the borders. For more complex light patterns, where different regions of the pattern have different local light

intensities, pulse-width modulation can be used to control the average light intensity experienced by each spot independently.

Off-focal plane aberration correction: We often presented a spatial photo-stimulation pattern based on glomerular shapes on the brain surface, while imaging deeper structures, such as mitral and tufted cells, which resulted in small, but significant changes in the size of the projected pattern (i.e. DMD-generated optogenetic stimulation pattern is in focus above the focal plane of the principal imaging objective). We compensated for this change in magnification by another linear transformation that we measured using the auxiliary microscope mounted beneath the principal microscope. The same procedure described above for mapping DMD-chip pixels to the primary camera (CCD1) was repeated using the secondary camera (CCD2) at several focal plane displacements in steps of 100 μm (e.g. 0, 100, 200…500 μm) and a corresponding set of transformations T(0),…, T(N) from the DMD-chip pixels to the secondary camera (CCD2) pixels was obtained. For each such transformation, we isolated the effect of changing displacement by multiplying the inverse of the zero-axial displacement transformation to obtain a set of "depth transformations" B(0),…, B(N). The depth transformation for arbitrary depths was calculated by linearly interpolating between the measured transformations.

Dichroic mirror offset: When registering the primary camera (CCD1), the dichroic mirror (DM2) must be positioned to direct light from the sample onto the primary camera. However, light from the DMD-chip is refracted as it passes through the dichroic mirror, causing the photo-stimulation pattern to be translated when DM2 is rotated by 90 degrees towards the PMT. We measured the displacement by projecting a square light pattern and recording an image with the auxiliary

681 microscope with the dichroic positioned towards the CCD1 or the PMT. Identifying a corner of
682 the projected square light pattern across the two images allowed using the secondary camera
683 CCD2-to-DMD-chip registration to determine the dichroic induced offset in projection.
684
685 **Lateral spot size measurement:** To calculate the full-width at half maximum (FWHM) in the
686 lateral direction (**Figs**. **2a-c**), we projected a circular spot onto a rhodamine B-coated coverslip and
687 acquired images with the auxiliary microscope. We thresholded each image and found the center
688 of the spot by computing a weighted centroid of the thresholded image:

689 $$c = argmax \sum_{x} I(x)x$$

690 where *x* is a vector containing the pixel coordinates and *I(x)* is the brightness of the image at point
691 *x*. The threshold was chosen heuristically by visual inspection of a single image and finding a value
692 which isolated the light spot, and which, when changed by small amounts, did not significantly
693 change the position of the centroid. We generated and averaged a set of line profiles passing
694 through the centroid rotated in 1° increments over 360°. The resulting symmetric line profile was
695 further used to compute the FWHM.
696
697 **Axial spot size measurement:** To measure the axial (z) profile of the projected light spots, we
698 brought different axial sections of the spots into the focal plane of CCD2 by stepping the principal
699 objective up and down over an interval of ± 100 µm (for spots of diameter ≤ 40 µm) or over ± 200
700 µm range (for spots of diameter > 40 µm) in z increments of 1 and 2 µm respectively. We defined
701 a region of interest (ROI) for analysis by taking all points within the FWHM of the spot in the
702 central section. The axial profile was defined as the intensity within the ROI across all sections
703 (**Figs**. **2a-c**). To estimate the effect of spherical and other types of aberrations, we measured the

axial profile of our projected spots for photo-stimulation plane z offsets of $\Delta z = 0 – 400$ µm with respect to the focal plane of the principal objective (**Fig. 3c**). For these measurements, we used spot diameters of 30, 60 and 90 µm respectively. Since in these configurations the diffuser is not positioned at a plane conjugate to the focal plane of the principal objective, any relative movement of the principal objective with respect to the tube lens L5 results in a slight change in magnification. The projected light spot size was corrected accordingly for the predicted increase in magnification.

Optical alignment. Alignment of the two-photon microscope followed the typical procedure[106]. The photo-stimulation beam was further aligned on the DMD chip. In our implementation, the DMD chip was mounted onto an articulating base-ball stage (SL20, Thorlabs) that can be raised and lowered. We used a periscope (RS99, Thorlabs) formed by two mirrors placed on kinematic mounts to center the photo-stimulation laser beam on the DMD chip. By applying an all-white pattern to the DMD-chip, a coarse alignment was obtained with the light reflected off the DMD-chip into the microscope and the photo-stimulation beam centered on the chip. One point of potential difficulty in the alignment procedure is given by the diffractive behavior of the DMD-chip when illuminated with coherent light. The face of each individual micro-mirror is offset with respect to the plane of the entire array of mirrors. Because of this, the DMD-chip behaves like a blazed diffraction grating. We aligned the blue laser beam such that most of the power is sent into a particular diffraction order. For a one-dimensional grating, the angle θ_m of diffraction order m is given by:

$$m\lambda = d(\sin\theta_i + \sin\theta_m)$$

while θ_r , the angle at which the reflected laser power leaves the DMD chip is given by:

$$\theta_r = 2\alpha - \theta_i$$

where θ_i is the incident angle with respect to the normal of the grating, λ is the wavelength, d is the grating spacing, and α is the offset or "blaze angle" of the mirror face relative to the grating. Since the micro-mirrors rotate along one diagonal of the mirror, the projection of the correct incident angle onto the mirror face must lie orthogonal to this diagonal. This line was determined by toggling all the mirrors between the on and off positions (setting an all-white or all-black image) and observing where the light is redirected.

To make final adjustments to the position, we compared the power in the brightest diffraction order to the four adjacent ones. We then adjusted the incident angle of the beam by tilting or translating the DMD-chip mount and compensating with the periscope mirrors to keep the photo-stimulation beam centered until the power in the brightest spot was maximally bright relatively to its neighbors. After optimizing the incident angle, the brightest spot was ~ 60% as powerful as before the DMD chip. A circular iris (SM2D25, Thorlabs) was used to block out light from other diffraction orders. Applying a cross-shaped or small circular pattern to the DMD chip is useful for determining the center of the field of stimulation. Finally, the dichroic mirror (DM1, **Fig. 1**) was used to align the center of the photo-stimulation pattern to the same vertical line as the two-photon beam, and the primary camera (CCD1) and PMTs were placed and aligned as described above.

Propagation of patterns through brain tissue: We used the auxiliary microscope to characterize how the lateral profile of the one photon extended (2D) photo-stimulation patterns deteriorates after propagation through brain slices of different thicknesses, following the procedure described in *Papagiakoumou et al., 2013*[77]. Adult mouse brains were fixed with paraformaldehyde and slices cut to various thicknesses. After focusing the photo-stimulation pattern on the fluorescent coverslip so that it was in focus on both the primary and the secondary cameras, we placed a slice on the top

of the coverslip with the pattern illuminating the olfactory bulb. The photo-stimulation light travelled through the slice and was scattered by the tissue before the pattern was imaged on the coverslip and the secondary camera (CCD2). We took a total of six measurements for each slice thickness (three positions, two slices). We used as reference for normalization the configuration when no slice was present (0 thickness) and defined the ROI for analysis as the set of points within the FWHM when no slice was present. We then calculated the light intensity and the standard deviation of pixel values within the ROI and compared it to values obtained for different slice thicknesses (**Figs**. **S2c-g**).

Phosphorescence artifacts. We observed a small slowly-decaying PMT signal upon illumination with the blue photo-stimulation laser in the absence of a fluorescence specimen. By progressively blocking off different parts of the optical path, we determined that the main contributors to this signal were the objective and tube lens (O and L5 in **Fig**. **1**). Upon replacing the N-BK7 glass tube lens (LA1384-A) with a fused silica lens (LA4545-A) with the same focal length, the signal dropped substantially (**Fig**. **S1e**). The artifact was not affected by the type of anti-reflective coating used (**Fig**. **S1e**). We tested several objectives (Olympus 20x 1.00 NA XLUMPlanFLN, Olympus 20x 0.95 XLUMPlanFL, Olympus 25x 1.05NA XLPlanN) and determined that they contributed differentially to this signal. Of these, the 25x fared best followed by the 1.0 NA 20x and the 0.95 NA 20x (data not shown). Following this optimization, when comparing identified cells to background areas in our imaging experiments, we could not detect any spurious signals in background selected areas.

Mice: For the *in vivo* experiments described here, we included data from 12 OMP-Cre x ReChr x Thy1GCaMP6s mice, 3 DAT-Cre mice and 4 DAT-Cre x Thy1-GCaMP6f mice. For experiments to map mitral/tufted cell parent glomeruli and identify *sister* cell cohorts, triple mouse crosses (OMP-Cre x Rosa26 CAG-LSL-ReaChR-mCitrine[79] x Thy1GCaMP6s_4.3[81]) were used to express ReaChR-mCitrine and GCaMP6f/s in the OSNs and respectively mitral and tufted cells (**Figs**. **4**,**5**). For experiments expressing ChR2 and GCaMP6f in DAT+ cells (**Fig**. **S5a-e**) , we used mice expressing Cre recombinase in DAT+ neurons and approximately 300 nl of a mixture of AAV (serotype 2.9, UNC Vector Core) virus carrying DIO-ChR2-mCherry and DIO-GCaMP6f was injected into the olfactory bulb at a depth of 300 µm as previously described[43]. For glomerular stimulation, for each light stimulus other than control stimuli, we fit a function of the form $f(d) = Ae^{-d/b}$ where f represents the light-evoked fluorescence change in a region of interest and d is the distance from that region to the center of the projected light mask. The width constant b of this exponential fit gives a measure of the spread of activity evoked by that stimulus. For each light intensity sampled, we repeated the analysis in two different fields of view, and the relationship between activation width and light intensity is shown in **Figs**. **S5b-e**. As in the case of OSN terminals photo-stimulation experiments, we flashed single 100 ms sub-glomerular light masks (20 µm diameter) between the imaging frames and recorded calcium transients in the DAT+ cells via multiphoton imaging. For analysis, the field of view was divided into a 20 by 20 grid (15 x 15 µm grid units), and the response was defined as the average change in fluorescence in each unit of the grid during the two frames (10 Hz) immediately following the light stimulus. We tested a range of photo-stimulation light intensities ranging from 0.5 to 10.0 mW/mm^2. We tuned up the intensity of the fluorescence response, while aiming to maintain spatial specificity, as indicated by the photo-activated area remaining largely confined to the chosen glomerulus. We quantified the

spread of activity by characterizing the relationship between the DAT+ cell response strength and the distance from the centroid of the light stimulus, which was well-fit by exponential decay. Within the range of light intensity used, the characteristic width constant varied from 25 µm for the lowest to 62 µm for the highest.

For experiments investigating the impact on mitral/tufted cell activity of glomerular GABAergic/DAT+-neurons (superficial short axon cells), DAT-Cre mice were crossed to Thy1GCaMP6f_5.11[81] mice (**Figs**. **6**, **S6**, **S7**). DAT-Cre x Thy1-GCaMP6f mice were retro-orbitally injected[107] with 5×10^{12} vp of AAV-PHP.eB:Syn-FLEX-rc[ChrimsonR-tdtomato], which was prepared as previously described[93,108]. Viral particles were diluted in saline to achieve a final volume of 100 µL per injected mouse. All animal procedures conformed to NIH guidelines and were approved by the Animal Care and Use Committee of Cold Spring Harbor Laboratory.

Surgical procedures: Mice were injected with NSAID Meloxicam 0.5 mg/Kg (Metacam®, Boehringer Ingelheim. Ingelheim, Germany) 24 hours prior the surgical procedure, at the onset of surgery, and for 2 days *post* each surgical procedure. Depending on the recovery progression, the NSAID treatment was maintained until mice showed alert, and responsive behavior. Before each stereotaxic surgery, mice were anesthetized with 10% v/v Isofluorane (Cat# 029405. Covetrus. Portland, ME, US). For the chronic window and headbar implantation procedures, mice were anesthetized with a ketamine/xylazine (125 mg/Kg - 12.5 mg/Kg) cocktail. During surgery, the animal's eyes were protected with an ophthalmic ointment (Puralube®. Dechra. Nortwich, England, UK). Temperature was maintained at 37 °C using a heating pad (FST TR-200, Fine Science Tools. Foster City, CA, USA). Respiratory rate and lack of pain reflexes were monitored

818 throughout the procedure. Chronic window implant surgeries were supplemented with
819 dexamethasone (4 mg/Kg) to prevent swelling, enrofloxacin (5 mg/Kg) to prevent bacterial
820 infection, and carprofen (5 mg/Kg) to reduce inflammation.
821
822 **Chronic implantations**: After recovery from the stereotaxic surgery, mice were implanted with a
823 custom titanium head bar attached with C&B Metabond Quick adhesive luting cement (Cat# S380.
824 Parkell. Edgewood, NY, USA), followed by black Ortho-JetTM dental acrylic application (Cat#
825 1520BLK. Lang. Chicago, IL, USA) and with a cranial window on top of the olfactory bulb as
826 previously described [109,110]. Special care was taken to remove the bone under the inter-frontal
827 suture and remove small bone pieces at the edges. During surgery, the exposed olfactory bulb was
828 continuously protected and cleaned of blood excess using artificial cerebrospinal fluid (aCSF) and
829 aCSF-soaked gelfoam. Once both hemibulbs were exposed and clean, a fresh drop of aCSF was
830 placed on top, followed by a 3 mm round cover glass, which was gently pushed onto the OB
831 surface to minimize motion artifacts in further experiments. Once in place, the coverslip was sealed
832 along the edges with a combination of VitrebondTM, Crazy-GlueTM, and dental acrylic to cover
833 the exposed skull. Mice recovered for ~ 7 days before imaging experiments.
834
835 **Odor delivery:** Odors were presented using a custom-built odor machine as described
836 elsewhere[85,111]. Undiluted or oil diluted (1:10 or 1:100) odorants were placed in glass vials and
837 airflow through the vials controlled by solenoid valves. The output odor stream was further mixed
838 with clean air in a 50:1 ratio, then this diluted stream was further mixed with clean air at a 5:1 ratio
839 before being sent through short teflon coated tubing placed in front of the mouse's snout. The 12
840 vials in the machine were split into three banks of four vials. Each bank could be independently

841 switched between sending odorized air and clean air to the mouse, in principle allowing
842 combinations of up to three odors. For assessing the effect of modulating GABA-ergic/DAT+
843 interneurons onto mitral and tufted cells responses, we used the following odors: isoamyl acetate,
844 acetaldehyde, valeraldehyde, allyl tiglate, ethyl heptanoate, heptanal, hexanol, 2-hexanone, ethyl
845 tiglate, 1,4 cineole, acetophenone.
846
847 **Data pre-processing**
848 **Movement correction and ROI selection:** Rigid registration in Fiji/ImageJ (template matching)
849 was applied to the acquired fluorescence time-lapse stacks. Images were visually inspected to
850 select a motion-free sequence of frames and create a mean reference image to which we registered
851 each image stack corresponding to a given trial. ROI selection was performed manually (ImageJ):
852 we used both the average and standard deviation projections of the registered images to draw ROIs
853 around the glomeruli and respectively mitral and tufted cell bodies in the FOV.
854
855 **Bleaching correction:** Post ROI extraction (glomeruli, mitral/tufted cells), we applied
856 fluorescence bleaching correction, assuming that: (1) bleaching follows a first order exponential
857 decay across trials for each individual ROI; (2) during the baseline period, any measured activity
858 is random. Given these assumptions, by averaging the fluorescence traces across trials of an ROI,
859 the only robust trend potentially present in the baseline is the characteristic bleaching for that ROI.
860 We checked that the baseline fluorescence of a given ROI is comparable across trials within a
861 session. The procedure used for each ROI was as follows: (1) we fitted an exponential decay
862 function to the fluorescence traces of individual trials, (2) subtracted the fitted function from the

ROI trace, (3) averaged the fluorescence traces across all trials for that ROI (aligned to stimulus presentation).

Normalization: For each ROI and trial, we normalized the traces individually, using a fluorescence baseline period (average of ten frames just before the stimulus onset as baseline fluorescence, F0). For each time point, fractional changes over the baseline fluorescence for the average trace were calculated as dF/F0.

ROI responsiveness and classification: On average, stimuli were presented across 4-5 repeats when imaging glomerular responses to optogenetic stimulation, and across 6-10 repeats when sampling the responses of mitral and tufted cells. To evaluate the responsiveness of each glomerulus, we obtained a distribution of average dF/F0 values from baseline periods, and used 95 percentile value of the distribution as response (significant signal) threshold. The baseline reference distribution was obtained from averaging dF/F0 values quantified over 10-frames intervals extracted from the baseline period and accumulated across all trials. For each ROI, we also obtained peak dF/F0 values during the optogenetic stimulation frames (1-2 frames). For each ROI, we compared the average response across trials with the baseline reference distribution. If this value crossed the 95^{th} percentile of the baseline distribution, the ROI was classified as responsive (*enhanced*).

To evaluate the responsiveness of each mitral and tufted cell, we searched for the peak of a monotonous response (signal) within 5 frames following optogenetic stimulation onset. Similarly, we obtained a distribution of average dF/F0 values from baseline periods using 4 frames just before the stimulation and accumulating across all trials. We compared the peak response value to the

standard deviation (SD) of the baseline. For calling *enhanced* responses, we used 4 SD of the baseline as response (significant signal) threshold; for calling *suppressed* responses, we used 3 SD of the baseline as response threshold to account for the intrinsic lower range of negative deflections from baseline. Cells that had slow and prolonged negative slope (<15º) with respect to baseline were not included in further analyses. To assess response reproducibility across trials, for each optogenetic stimulation mask, for each trial, we built a *trial response vector* (using 5-frames from the stimulus onset) and computed the Pearson correlation with respect to the response vectors of the other trials. If for a given trial the average correlation with respect to the response vectors of the other trials, the trial was rejected. For an ROI to be considered for further analysis, at least 2 repeats had to pass the criterion. Cells that had slow responses, which occurred only after offset of light stimulation were not included for further analysis to minimize the contribution of disinhibitory effects across the bulb network.

Self-response correlations: To obtain a measure of reliability for ensemble mitral cell responses across different trials to the same DAT+ glomerular photo-stimulation mask, and respectively to the same odorant, using bootstrapping (50 times) in each iteration split the trials into two random subsets of trials, and calculated 'self' response correlations, whose average values were 0.81 ± 0.14 for light masks and 0.87 ± 0.10 for odor responses of the same MC ensembles (**Fig**. **S5b**).

For each mitral and tufted cells, the *odor responses* (**Fig**. **6**) were calculated as described above using 10-frames periods to build a distribution of baseline values and accumulating across trials. We also used 10-frames periods starting from stimulus onset to search for the response peak. To calculate the *light modulation of the odor response* to DAT+ glomerular photo-stimulation masks

(**Figs**. **6f-h**, **S7**), we used as reference the frame just before light stimulation onset. We asked whether in the 2 frames following light onset, we could identify a significant increase/dip in signal compared to this reference dF/F value. A change in signal (defined delta between reference and signal during light stimulation) was considered significant if it amounted to more than 10% of the average peak odor response amplitude (preceding light onset), and was also larger than 3 SDs of the baseline fluorescence (preceding odor onset). To assess response reproducibility across trials, for each stimulus, we performed correlation analysis across trials as described above.

Assessing glomerular response spatial extent and specificity: In **Fig**. **S3c** *i* (Right), for each photo-stimulation mask, we normalized the sum total area of the significantly responsive glomerular pixels. We multiplied the sum total area of these responsive pixels by the ratio between the area of the photo-stimulation mask and the surface area of target glomerulus surface. We defined the anatomical outline of each glomerulus in the field of view manually using its baseline fluorescence. To determine the specificity of glomerular responses across light intensities we computed two metrics. First (blue trace, **Fig. 4f**), we normalized responsive pixels within the boundaries of the target glomerulus by all responsive pixels located within the boundaries of any glomeruli across the FOV. Second (red trace, **Fig**. **4f**), we normalized the significantly responsive pixels within the target glomerulus by the sum area of all responsive pixels within the FOV, including those spanning the juxtaglomerular space, surrounding the glomeruli.

Correlation analysis and shuffled controls: For each pairwise correlation analysis (**Figs**. **6e**,**h**, **S5b**, **S7e-f**), we ran 15 repetitions of the shuffling controls and compared the experimental data with the shuffled data (Wilcoxon signed-rank test).

Statistical tests: Depending on the properties of the analyzed data, different statistical tests were used to evaluate the differences between data groups. The information for each statistical comparison is detailed in the legends of each figure panel. 'Two-sample unpaired Student's t-test' was used to evaluate significant differences in the means of two normally distributed data sets. 'The normality of the data distribution was checked using a 'One-sample Kolmogorov-Smirnov test' for each data group before the testing differences with the 'Student's t-test'. A two-tailed 95% confidence interval was used for both Student's t-test. Significant differences between two non-normally distributed data sets were evaluated with a nonparametric 'Wilcoxon signed-rank test.' The linear correlation between two data sets was assessed by computing the Pearson correlation coefficient. When needed, the coefficient of determination (R^2) was used to evaluate how well the compared data sets fit a linear regression model. All the statistical comparisons were tested using MATLAB® using the following functions for each test: 'Two-sample unpaired Student's t-test': ttest; 'One-sample Kolmogorov-Smirnov test': kstest; 'Multiple comparisons of means test': multcompare; 'Two-sample Kolmogorov-Smirnov test': kstest2; 'Pearson correlation coefficient': corrcoef. 'Wilcoxon signed-Rank': signrank.

References

1. Scanziani, M. & Häusser, M. Electrophysiology in the age of light. *Nature* **461**, 930–939 (2009).
2. Emiliani, V., Cohen, A. E., Deisseroth, K. & Häusser, M. All-Optical Interrogation of Neural Circuits. *J. Neurosci.* **35**, 13917–13926 (2015).
3. Peron, S. & Svoboda, K. From cudgel to scalpel: toward precise neural control with optogenetics. *Nat. Methods* **8**, 30–34 (2011).
4. Prakash, R. *et al.* Two-photon optogenetic toolbox for fast inhibition, excitation and bistable modulation. *Nat. Methods* **9**, 1171–1179 (2012).
5. Adesnik, H. & Abdeladim, L. Probing neural codes with two-photon holographic optogenetics. *Nat. Neurosci.* **24**, 1356–1366 (2021).
6. Lutz, C. *et al.* Holographic photolysis of caged neurotransmitters. *Nat. Methods* **5**, 821–827 (2008).
7. Nikolenko, V. *et al.* SLM Microscopy: Scanless Two-Photon Imaging and Photostimulation with Spatial Light Modulators. *Front. Neural Circuits* **2**, 5 (2008).
8. Packer, A. M. *et al.* Two-photon optogenetics of dendritic spines and neural circuits. *Nat. Methods* **9**, 1202–1205 (2012).
9. Packer, A. M., Russell, L. E., Dalgleish, H. W. P. & Häusser, M. Simultaneous all-optical manipulation and recording of neural circuit activity with cellular resolution in vivo. *Nat. Methods* **12**, 140–146 (2015).
10. Carrillo-Reid, L., Yang, W., Bando, Y., Peterka, D. S. & Yuste, R. Imprinting and recalling cortical ensembles. *Science* **353**, 691–694 (2016).

11. Yang, W., Carrillo-Reid, L., Bando, Y., Peterka, D. S. & Yuste, R. Simultaneous two-photon imaging and two-photon optogenetics of cortical circuits in three dimensions. *eLife* **7**, e32671 (2018).
12. Papagiakoumou, E. *et al.* Scanless two-photon excitation of channelrhodopsin-2. *Nat. Methods* **7**, 848–854 (2010).
13. Papagiakoumou, E., Ronzitti, E. & Emiliani, V. Scanless two-photon excitation with temporal focusing. *Nat. Methods* **17**, 571–581 (2020).
14. Villette, V. *et al.* Ultrafast Two-Photon Imaging of a High-Gain Voltage Indicator in Awake Behaving Mice. *Cell* **179**, 1590-1608.e23 (2019).
15. Fan, L. Z. *et al.* All-optical physiology resolves a synaptic basis for behavioral timescale plasticity. *Cell* **186**, 543-559.e19 (2023).
16. Anselmi, F., Ventalon, C., Bègue, A., Ogden, D. & Emiliani, V. Three-dimensional imaging and photostimulation by remote-focusing and holographic light patterning. *Proc. Natl. Acad. Sci. U. S. A.* **108**, 19504–19509 (2011).
17. Anselmi, F., Banerjee, A. & Albeanu, D. F. Patterned Photostimulation in the Brain. in *New Techniques in Systems Neuroscience* (ed. Douglass, A. D.) 235–270 (Springer International Publishing, Cham, 2015).
18. Andrasfalvy, B. K., Zemelman, B. V., Tang, J. & Vaziri, A. Two-photon single-cell optogenetic control of neuronal activity by sculpted light. *Proc. Natl. Acad. Sci. U. S. A.* **107**, 11981–11986 (2010).
19. Rickgauer, J. P., Deisseroth, K. & Tank, D. W. Simultaneous cellular-resolution optical perturbation and imaging of place cell firing fields. *Nat. Neurosci.* **17**, 1816–1824 (2014).

20. Grewe, B. F., Voigt, F. F., van 't Hoff, M. & Helmchen, F. Fast two-layer two-photon imaging of neuronal cell populations using an electrically tunable lens. *Biomed. Opt. Express* **2**, 2035–2046 (2011).
21. Sheffield, M. E. J. & Dombeck, D. A. Calcium transient prevalence across the dendritic arbour predicts place field properties. *Nature* **517**, 200–204 (2015).
22. Iwai, D., Izawa, H., Kashima, K., Ueda, T. & Sato, K. Speeded-Up Focus Control of Electrically Tunable Lens by Sparse Optimization. *Sci. Rep.* **9**, 12365 (2019).
23. Katona, G. *et al.* Fast two-photon in vivo imaging with three-dimensional random-access scanning in large tissue volumes. *Nat. Methods* **9**, 201–208 (2012).
24. Iyer, V., Losavio, B. E. & Saggau, P. Compensation of spatial and temporal dispersion for acousto-optic multiphoton laser-scanning microscopy. *J. Biomed. Opt.* **8**, 460 (2003).
25. Duemani Reddy, G., Kelleher, K., Fink, R. & Saggau, P. Three-dimensional random access multiphoton microscopy for functional imaging of neuronal activity. *Nat. Neurosci.* **11**, 713–720 (2008).
26. Salomé, R. *et al.* Ultrafast random-access scanning in two-photon microscopy using acousto-optic deflectors. *J. Neurosci. Methods* **154**, 161–174 (2006).
27. Akemann, W. *et al.* Fast optical recording of neuronal activity by three-dimensional custom-access serial holography. *Nat. Methods* **19**, 100–110 (2022).
28. Hernandez, O., Pietrajtis, K., Mathieu, B. & Dieudonné, S. Optogenetic stimulation of complex spatio-temporal activity patterns by acousto-optic light steering probes cerebellar granular layer integrative properties. *Sci. Rep.* **8**, 13768 (2018).
29. Hernandez, O. *et al.* Three-dimensional spatiotemporal focusing of holographic patterns. *Nat. Commun.* **7**, 11928 (2016).

30. Oron, D., Papagiakoumou, E., Anselmi, F. & Emiliani, V. Two-photon optogenetics. *Prog. Brain Res.* **196**, 119–143 (2012).

31. Russell, L. E. *et al.* All-optical interrogation of neural circuits in behaving mice. *Nat. Protoc.* **17**, 1579–1620 (2022).

32. Ronzitti, E., Emiliani, V. & Papagiakoumou, E. Methods for Three-Dimensional All-Optical Manipulation of Neural Circuits. *Front. Cell. Neurosci.* **12**, 469 (2018).

33. Pégard, N. C. *et al.* Three-dimensional scanless holographic optogenetics with temporal focusing (3D-SHOT). *Nat. Commun.* **8**, 1228 (2017).

34. Petreanu, L., Huber, D., Sobczyk, A. & Svoboda, K. Channelrhodopsin-2–assisted circuit mapping of long-range callosal projections. *Nat. Neurosci.* **10**, 663–668 (2007).

35. Katz, L. C. & Dalva, M. B. Scanning laser photostimulation: a new approach for analyzing brain circuits. *J. Neurosci. Methods* **54**, 205–218 (1994).

36. Dhawale, A. K., Hagiwara, A., Bhalla, U. S., Murthy, V. N. & Albeanu, D. F. Non-redundant odor coding by sister mitral cells revealed by light addressable glomeruli in the mouse. *Nat Neurosci* **13**, 1404–1412 (2010).

37. Chong, E. *et al.* Manipulating synthetic optogenetic odors reveals the coding logic of olfactory perception. *Science* **368**, (2020).

38. Guo, Z. V., Hart, A. C. & Ramanathan, S. Optical interrogation of neural circuits in Caenorhabditis elegans. *Nat. Methods* **6**, 891–896 (2009).

39. Blumhagen, F. *et al.* Neuronal filtering of multiplexed odour representations. *Nature* **479**, 493–498 (2011).

40. Zhu, P., Fajardo, O., Shum, J., Zhang Schärer, Y.-P. & Friedrich, R. W. High-resolution optical control of spatiotemporal neuronal activity patterns in zebrafish using a digital micromirror device. *Nat. Protoc.* **7**, 1410–1425 (2012).
41. Wyart, C. *et al.* Optogenetic dissection of a behavioural module in the vertebrate spinal cord. *Nature* **461**, 407–410 (2009).
42. Zhu, P., Frank, T. & Friedrich, R. W. Equalization of odor representations by a network of electrically coupled inhibitory interneurons. *Nat. Neurosci.* **16**, 1678–1686 (2013).
43. Banerjee, A. *et al.* An Interglomerular Circuit Gates Glomerular Output and Implements Gain Control in the Mouse Olfactory Bulb. *Neuron* **87**, 193–207 (2015).
44. Leifer, A. M., Fang-Yen, C., Gershow, M., Alkema, M. J. & Samuel, A. D. T. Optogenetic manipulation of neural activity in freely moving Caenorhabditis elegans. *Nat. Methods* **8**, 147–152 (2011).
45. Arrenberg, A. B., Stainier, D. Y. R., Baier, H. & Huisken, J. Optogenetic control of cardiac function. *Science* **330**, 971–974 (2010).
46. Farah, N., Reutsky, I. & Shoham, S. Patterned optical activation of retinal ganglion cells. *Conf. Proc. Annu. Int. Conf. IEEE Eng. Med. Biol. Soc. IEEE Eng. Med. Biol. Soc. Conf.* **2007**, 6368–6370 (2007).
47. Fast and light-efficient remote focusing for volumetric voltage imaging | Nature Communications. https://www.nature.com/articles/s41467-024-53685-5#Bib1.
48. Botcherby, E. J., Juškaitis, R., Booth, M. J. & Wilson, T. An optical technique for remote focusing in microscopy. *Opt. Commun.* **281**, 880–887 (2008).
49. Botcherby, E. J. *et al.* Aberration-free three-dimensional multiphoton imaging of neuronal activity at kHz rates. *Proc. Natl. Acad. Sci. U. S. A.* **109**, 2919–2924 (2012).

50. Rapid 3D light-sheet microscopy with a tunable lens. https://opg.optica.org/oe/fulltext.cfm?uri=oe-21-18-21010&id=260811.

51. Shain, W. J., Vickers, N. A., Goldberg, B. B., Bifano, T. & Mertz, J. Extended depth-of-field microscopy with a high-speed deformable mirror. *Opt. Lett.* **42**, 995–998 (2017).

52. Remote z-scanning with a macroscopic voice coil motor for fast 3D multiphoton laser scanning microscopy. https://opg.optica.org/boe/fulltext.cfm?uri=boe-7-5-1656&id=338741.

53. Shepherd, G. M. Synaptic organization of the mammalian olfactory bulb. *Physiol. Rev.* **52**, 864–917 (1972).

54. Wilson, R. I. & Mainen, Z. F. Early events in olfactory processing. *Annu. Rev. Neurosci.* **29**, 163–201 (2006).

55. Arneodo, E. M. *et al.* Stimulus dependent diversity and stereotypy in the output of an olfactory functional unit. *Nat. Commun.* **9**, 1347 (2018).

56. Kikuta, S., Fletcher, M. L., Homma, R., Yamasoba, T. & Nagayama, S. Odorant response properties of individual neurons in an olfactory glomerular module. *Neuron* **77**, 1122–1135 (2013).

57. Padmanabhan, K. & Urban, N. N. Intrinsic biophysical diversity decorrelates neuronal firing while increasing information content. *Nat. Neurosci.* **13**, 1276–1282 (2010).

58. Schwarz, D. *et al.* Architecture of a mammalian glomerular domain revealed by novel volume electroporation using nanoengineered microelectrodes. *Nat. Commun.* **9**, 1–14 (2018).

59. Odour responses of sister projection neurons in the mouse olfactory bulb, revealed by correlative two-photon imaging and synchrotron X-ray holographic nano-tomography. https://www.abstractsonline.com/pp8/#!/10892/presentation/40650.

60. Functional interactions between olfactory circuits shapes the timing and structure of odor representations. https://www.abstractsonline.com/pp8/#!/10892/presentation/40671.

61. Tootoonian, S., Schaefer, A. T. & Latham, P. E. Sparse connectivity for MAP inference in linear models using sister mitral cells. *PLoS Comput. Biol.* **18**, e1009808 (2022).

62. Tan, J., Savigner, A., Ma, M. & Luo, M. Odor information processing by the olfactory bulb analyzed in gene-targeted mice. *Neuron* **65**, 912–926 (2010).

63. Buonviso, N. & Chaput, M. A. Response similarity to odors in olfactory bulb output cells presumed to be connected to the same glomerulus: electrophysiological study using simultaneous single-unit recordings. *J. Neurophysiol.* **63**, 447–454 (1990).

64. Schoppa, N. E. & Westbrook, G. L. Glomerulus-specific synchronization of mitral cells in the olfactory bulb. *Neuron* **31**, 639–651 (2001).

65. Chen, T.-W., Lin, B.-J. & Schild, D. Odor coding by modules of coherent mitral/tufted cells in the vertebrate olfactory bulb. *Proc. Natl. Acad. Sci. U. S. A.* **106**, 2401–2406 (2009).

66. Aungst, J. L. *et al.* Centre-surround inhibition among olfactory bulb glomeruli. *Nature* **426**, 623–629 (2003).

67. Zavitz, D., Youngstrom, I. A., Borisyuk, A. & Wachowiak, M. Effect of Interglomerular Inhibitory Networks on Olfactory Bulb Odor Representations. *J. Neurosci. Off. J. Soc. Neurosci.* **40**, 5954–5969 (2020).

68. Olsen, S. R., Bhandawat, V. & Wilson, R. I. Divisive normalization in olfactory population codes. *Neuron* **66**, 287–299 (2010).

69. Cleland, T. A. Early transformations in odor representation. *Trends Neurosci.* **33**, 130–139 (2010).

70. Lyons-Warren, A. M. *et al.* Co-transmitting interneurons in the mouse olfactory bulb regulate olfactory detection and discrimination. *Cell Rep.* **42**, 113471 (2023).

71. Kiyokage, E. *et al.* Molecular identity of periglomerular and short axon cells. *J. Neurosci. Off. J. Soc. Neurosci.* **30**, 1185–1196 (2010).

72. Whitesell, J. D., Sorensen, K. A., Jarvie, B. C., Hentges, S. T. & Schoppa, N. E. Interglomerular lateral inhibition targeted on external tufted cells in the olfactory bulb. *J. Neurosci. Off. J. Soc. Neurosci.* **33**, 1552–1563 (2013).

73. Liu, S., Plachez, C., Shao, Z., Puche, A. & Shipley, M. T. Olfactory bulb short axon cell release of GABA and dopamine produces a temporally biphasic inhibition-excitation response in external tufted cells. *J. Neurosci. Off. J. Soc. Neurosci.* **33**, 2916–2926 (2013).

74. Liu, S., Puche, A. C. & Shipley, M. T. The Interglomerular Circuit Potently Inhibits Olfactory Bulb Output Neurons by Both Direct and Indirect Pathways. *J. Neurosci. Off. J. Soc. Neurosci.* **36**, 9604–9617 (2016).

75. Papagiakoumou, E., de Sars, V., Oron, D. & Emiliani, V. Patterned two-photon illumination by spatiotemporal shaping of ultrashort pulses. *Opt. Express* **16**, 22039–22047 (2008).

76. Bègue, A. *et al.* Two-photon excitation in scattering media by spatiotemporally shaped beams and their application in optogenetic stimulation. *Biomed. Opt. Express* **4**, 2869–2879 (2013).

77. Papagiakoumou, E. *et al.* Functional patterned multiphoton excitation deep inside scattering tissue. *Nat. Photonics* **7**, 274–278 (2013).

78. Fukunaga, I., Berning, M., Kollo, M., Schmaltz, A. & Schaefer, A. T. Two distinct channels of olfactory bulb output. *Neuron* **75**, 320–329 (2012).

79. Hooks, B. M., Lin, J. Y., Guo, C. & Svoboda, K. Dual-Channel Circuit Mapping Reveals Sensorimotor Convergence in the Primary Motor Cortex. *J. Neurosci.* **35**, 4418–4426 (2015).

80. Chen, T.-W. *et al.* Ultrasensitive fluorescent proteins for imaging neuronal activity. *Nature* **499**, 295–300 (2013).

81. Dana, H. *et al.* Thy1 transgenic mice expressing the red fluorescent calcium indicator jRGECO1a for neuronal population imaging in vivo. *PloS One* **13**, e0205444 (2018).

82. Mombaerts, P. Axonal wiring in the mouse olfactory system. *Annu. Rev. Cell Dev. Biol.* **22**, 713–737 (2006).

83. Chae, H. *et al.* Mosaic representations of odors in the input and output layers of the mouse olfactory bulb. *Nat. Neurosci.* **22**, 1306–1317 (2019).

84. Fantana, A. L., Soucy, E. R. & Meister, M. Rat olfactory bulb mitral cells receive sparse glomerular inputs. *Neuron* **59**, 802–814 (2008).

85. Gupta, P., Albeanu, D. F. & Bhalla, U. S. Olfactory bulb coding of odors, mixtures and sniffs is a linear sum of odor time profiles. *Nat. Neurosci.* **18**, 272–281 (2015).

86. Adrian, E. D. Olfactory reactions in the brain of the hedgehog. *J. Physiol.* **100**, 459–473 (1942).

87. Galliano, E. *et al.* Embryonic and postnatal neurogenesis produce functionally distinct subclasses of dopaminergic neuron. *eLife* **7**, e32373 (2018).

88. Economo, M. N., Hansen, K. R. & Wachowiak, M. Control of Mitral/Tufted Cell Output by Selective Inhibition among Olfactory Bulb Glomeruli. *Neuron* **91**, 397–411 (2016).

89. Niessing, J. & Friedrich, R. W. Olfactory pattern classification by discrete neuronal network states. *Nature* **465**, 47–52 (2010).

90. Wanner, A. A. & Friedrich, R. W. Whitening of odor representations by the wiring diagram of the olfactory bulb. *Nat. Neurosci.* **23**, 433–442 (2020).

1147 91. Boyden, E. S., Zhang, F., Bamberg, E., Nagel, G. & Deisseroth, K. Millisecond-timescale,
1148 genetically targeted optical control of neural activity. *Nat Neurosci* **8**, 1263–1268 (2005).
1149 92. Tian, L. *et al.* Imaging neural activity in worms, flies and mice with improved GCaMP calcium
1150 indicators. *Nat Meth* **6**, 875–881 (2009).
1151 93. Chan, K. Y. *et al.* Engineered AAVs for efficient noninvasive gene delivery to the central and
1152 peripheral nervous systems. *Nat. Neurosci.* **20**, 1172–1179 (2017).
1153 94. Klapoetke, N. C. *et al.* Independent optical excitation of distinct neural populations. *Nat.*
1154 *Methods* **11**, 338–346 (2014).
1155 95. Kebschull, J. M. *et al.* High-Throughput Mapping of Single-Neuron Projections by
1156 Sequencing of Barcoded RNA. *Neuron* **91**, 975–987 (2016).
1157 96. Chen, Y. *et al.* High-throughput sequencing of single neuron projections reveals spatial
1158 organization in the olfactory cortex. *Cell* **185**, 4117-4134.e28 (2022).
1159 97. Petersen, C. C. H. Sensorimotor processing in the rodent barrel cortex. *Nat. Rev. Neurosci.* **20**,
1160 533–546 (2019).
1161 98. Han, Y. *et al.* The logic of single-cell projections from visual cortex. *Nature* **556**, 51–56
1162 (2018).
1163 99. Glickfeld, L. L., Andermann, M. L., Bonin, V. & Reid, R. C. Cortico-cortical projections in
1164 mouse visual cortex are functionally target specific. *Nat. Neurosci.* **16**, 219–226 (2013).
1165 100. Orsolic, I., Rio, M., Mrsic-Flogel, T. D. & Znamenskiy, P. Mesoscale cortical dynamics
1166 reflect the interaction of sensory evidence and temporal expectation during perceptual
1167 decision-making. *Neuron* **109**, 1861-1875.e10 (2021).
1168 101. Leinweber, M., Ward, D. R., Sobczak, J. M., Attinger, A. & Keller, G. B. A Sensorimotor
1169 Circuit in Mouse Cortex for Visual Flow Predictions. *Neuron* **96**, 1204 (2017).

1170 102. Attinger, A., Wang, B. & Keller, G. B. Visuomotor Coupling Shapes the Functional
1171 Development of Mouse Visual Cortex. *Cell* **169**, 1291-1302.e14 (2017).
1172 103. Schneider, D. M., Nelson, A. & Mooney, R. A synaptic and circuit basis for corollary
1173 discharge in the auditory cortex. *Nature* **513**, 189–194 (2014).
1174 104. Schneider, D. M., Sundararajan, J. & Mooney, R. A cortical filter that learns to suppress
1175 the acoustic consequences of movement. *Nature* **561**, 391–395 (2018).
1176 105. Campbell, R. A. A., Eifert, R. W. & Turner, G. C. Openstage: a low-cost motorized
1177 microscope stage with sub-micron positioning accuracy. *PloS One* **9**, e88977 (2014).
1178 106. (PDF) Principles, Design, and Construction of a Two-Photon Laser Scanning Microscope
1179 for In Vitro and In Vivo Brain Imaging.
1180 https://www.researchgate.net/publication/233870537_Principles_Design_and_Construction_
1181 of_a_Two-
1182 Photon_Laser_Scanning_Microscope_for_In_Vitro_and_In_Vivo_Brain_Imaging.
1183 107. Yardeni, T., Eckhaus, M., Morris, H. D., Huizing, M. & Hoogstraten-Miller, S. Retro-
1184 orbital injections in mice. *Lab Anim.* **40**, 155–160 (2011).
1185 108. Challis, R. C. *et al.* Systemic AAV vectors for widespread and targeted gene delivery in
1186 rodents. *Nat. Protoc.* **14**, 379–414 (2019).
1187 109. Otazu, G. H., Chae, H., Davis, M. B. & Albeanu, D. F. Cortical Feedback Decorrelates
1188 Olfactory Bulb Output in Awake Mice. *Neuron* **86**, 1461–1477 (2015).
1189 110. Chae, H., Banerjee, A., Dussauze, M. & Albeanu, D. F. Long-range functional loops in the
1190 mouse olfactory system and their roles in computing odor identity. *Neuron* **0**, (2022).

1191 111. Gupta, P., Albeanu, D. F. & Bhalla, U. S. An odor delivery system for arbitrary time-
1192 varying patterns of odors, mixtures and concentrations. *bioRxiv* 077875 (2016)
1193 doi:10.1101/077875.